ACCEPTED FOR PUBLICATION IN THE ASTROPHYSICAL JOURNAL
Preprint typeset using LaTeX style emulateapj v. 6/22/04

arXiv:astro-ph/0501088v1 6 Jan 2005

THE ASSEMBLY OF DIVERSITY IN THE MORPHOLOGIES AND STELLAR POPULATIONS OF HIGH–REDSHIFT GALAXIES[1]

CASEY PAPOVICH
Steward Observatory, University of Arizona, 933 North Cherry Avenue, Tucson, AZ 85721; papovich@as.arizona.edu

MARK DICKINSON[2,3]
National Optical Astronomy Observatory, 950 North Cherry Avenue, Tucson, AZ 85719; med@noao.edu

MAURO GIAVALISCO
Space Telescope Science Institute, 3700 San Martin Drive, Baltimore, MD 21218; mauro@stsci.edu

CHRISTOPHER J. CONSELICE[4]
Palomar Observatory, California Institute of Technology, MS 105–24, Pasadena, CA 91125; cc@astro.caltech.edu

AND

HENRY C. FERGUSON[3]
Space Telescope Science Institute, 3700 San Martin Drive, Baltimore, MD 21218; ferguson@stsci.edu
Accepted for Publication in the Astrophysical Journal

ABSTRACT

We have used deep images from the *Hubble Space Telescope* to study the evolution in the morphologies, sizes, stellar–masses, colors, and internal color dispersion of galaxies in the Hubble Deep Field North. We selected two galaxy samples at $0.7 \leq z \leq 1.4$ and $1.9 \leq z \leq 3.0$ from a near–infrared, flux–limited catalog with complete photometric and spectroscopic redshift information. At $z \sim 1$ the majority of galaxies with $M(B) \leq -20.5$ have rest–frame optical morphologies of early–to–mid-type Hubble–sequence galaxies, and many galaxies show strong transformations between their rest–frame UV and optical morphologies. In stark contrast, galaxies at $z \sim 2.3$ all have compact and irregular rest–frame optical morphologies with little difference between their rest–frame UV–optical morphologies, and with no clearly evident Hubble–sequence candidates. The mean galaxy size increases from $z \sim 2.3$ to 1 by roughly 40%, and the number density of galaxies larger than 3 kpc increases by a factor of ≈ 7. The size–luminosity distribution of $z \sim 1$ galaxies is broadly consistent with that in the local universe, allowing for passive evolution. However, we argue that galaxies at $z \sim 2.3$ are not the fully formed progenitors of present–day galaxies, and they must continue to grow in both their sizes and stellar masses. We have quantified the differences in morphology by measuring the galaxies' internal UV–optical color dispersion, which constrains the amount of current star–formation relative to older stellar populations. The mean and scatter in the galaxies' UV–optical total colors and internal color dispersion increase from $z \sim 2.3$ to 1. At $z \sim 1$ many galaxies with large internal color dispersion are spirals, with a few irregular and interacting systems. Few $z \sim 2.3$ galaxies have high internal color dispersion, and we infer that those that do are also actively merging. Using simple models, we interpret the change in the total color and internal color dispersion as evidence for the presence of older and more diverse stellar populations at $z \sim 1$ that are not generally present at $z \gtrsim 2$. The $z \sim 2.3$ galaxies do not increase their stellar diversity as rapidly as they could given basic timescale arguments and simple models. We conclude that the star–formation histories of galaxies at $z \gtrsim 2$ are dominated by discrete, recurrent starbursts, which quickly homogenize the galaxies' stellar content and are possibly associated with mergers. The increase in the diversification of stellar populations by $z \sim 1$ implies that merger–induced starbursts occur less frequently than at higher redshifts, and more quiescent modes of star–formation become the dominant mechanism. This transition in the mode of star formation coincides with the emergence of Hubble–sequence galaxies, which seems to occur around $z \sim 1.4$.

Subject headings: cosmology: observations — galaxies: evolution — galaxies: formation — galaxies: high-redshift — galaxies: stellar content — galaxies: structure

1. INTRODUCTION

Galaxy morphologies stem from complex formation and evolutionary records. The fact that present–day galaxies span such a great range of morphological type and that galaxy morphology correlates with optical luminosity, color, size, and mass (e.g., Roberts & Haynes 1994) indicates that galaxy appearances depend strongly on their assembly histories. The quantitative study of the morphological properties of galaxies at high redshifts has advanced rapidly due primarily to the high–angular resolution of the *Hubble Space Telescope* (*HST*). The *HST* instruments provide imaging with angular resolution of $\sim 0\farcs1$, which corresponds to physical scales of less than 1 kpc for cosmologically distant galaxies.

Many surveys using *HST* imaging have broadly shown that while the local Hubble Sequence seems to exist for $z \lesssim 1 - 1.5$ (e.g., van den Bergh et al. 1996;

[1] Based on observations taken with the NASA/ESA Hubble Space Telescope, which is operated by the Association of Universities for Research in Astronomy, Inc. (AURA) under NASA contract NAS5–26555. These observations are associated with programs GO/DD–6337 and GO–7817.

[2] also Space Telescope Science Institute

[3] also Department of Physics and Astronomy; The Johns Hopkins University, 3400 N. Charles St., Baltimore, MD 21218

[4] NSF Fellow

van den Bergh, Cohen, & Crabbe 2001; Griffiths et al. 1996; Brinchmann et al. 1998; Lilly et al. 1998; Simard et al. 1999; van Dokkum et al. 2000; Stanford et al. 2004; Ravindranath et al. 2004), the morphological mix of galaxies at these redshifts shows an increase in the abundance of irregular and peculiar galaxies, particularly at fainter magnitudes (e.g. Driver, Windhorst, & Griffiths 1995; Ellis 1997; Brinchmann et al. 1998; Brinchmann & Ellis 2000). However, the formation and evolution of such systems is unclear. Several studies have concluded that a large fraction of giant spiral and other early–type galaxies were already in place by moderate redshifts (van den Bergh et al. 1996; Abraham et al. 1996; Brinchmann et al. 1998; Lilly et al. 1998; Im et al. 1999; Simard et al. 1999; Im et al. 2002; Moustakas et al. 2004; Ravindranath et al. 2004; Stanford et al. 2004) and that the characteristic galaxy size has changed little since $z \sim 1$ (Lilly et al. 1998). Moreover, little discernible evolution is evident in such systems even when uncertainties in the morphological classification and other selection effects are included (Marleau & Simard 1998; Simard et al. 1999; Ravindranath et al. 2004), which reinforces the conclusion that some fraction of the Hubble–sequence galaxy population had assembled by $z \sim 1$.

How these large, symmetric Hubble–sequence galaxies form and assemble their diverse stellar populations remains enigmatic. Logically, they descend from higher–redshift progenitors, but it is difficult to link the populations. The Hubble sequence seems to no longer apply at $z \gtrsim 1.5-2$ (van den Bergh et al. 2001; van den Bergh 2002). The observed morphologies of galaxies at $z \gtrsim 2$ are generally highly irregular or centrally compact (Giavalisco, Steidel, & Macchetto 1996; Lowenthal et al. 1997; Dickinson 2000; Daddi et al. 2004), but some large disk–galaxy candidates exist (e.g., Labbé et al. 2003; Conselice et al. 2004b). The sizes, spatial densities, and stellar masses of galaxies at these redshifts are comparable to those of present–day bulges and lower–redshift galactic spheroidal components (Giavalisco et al. 1996, 1998; Lowenthal et al. 1997; Giavalisco & Dickinson 2001; Papovich, Dickinson, & Ferguson 2001; Shapley et al. 2001), and thus it is tempting to equate them with a one–to–one correspondence. However, the space density of galaxies at $z \sim 2-3$ may be inconsistent with the fraction of bulge–dominated galaxies observed at moderate redshift ($z \sim 1$) in the HDF–N (Marleau & Simard 1998). Moreover, although the stellar–mass density at $z \sim 1$ is dominated by red, evolved galaxies (Bell et al. 2004), the majority of the galaxy stellar mass at $z \gtrsim 2$ exists in blue, irregular galaxies (e.g., Dickinson et al. 2003; Conselice, Blackburne, & Papovich 2004a) with some contribution from dust–enshrouded, massive starbursts (Förster–Schreiber et al. 2004; van Dokkum et al. 2004).

The physical processes that govern how galaxies observed at $z \gtrsim 2$ evolve into galaxies at more modest redshifts ($z \sim 1$) are poorly understood. This is partly due to difficulties in comparing the properties of galaxies observed at different rest–frame wavelengths and with different telescope and detector combinations. It is entirely expected that all observable galaxy properties (e.g., luminosities, colors, masses, morphologies, densities) evolve substantially over galaxies' lifetimes, and the subsequent observational biases further frustrate studies of galaxy evolution when examining galaxy populations based on some selection criteria.

One complication in the studies of galaxy morphology results from the fact that a fixed bandpass samples lower rest–frame wavelengths with increasing redshift. For example, observations at optical wavelengths probe only the rest–frame UV portions of the spectral energy distributions (SEDs) of galaxies at $z \gtrsim 1$, and there is little relation between rest-frame UV and optical properties of galaxies. Local galaxies have been shown to exhibit strong transformations between their morphologies at rest–frame UV and optical wavelengths (see, e.g. Kuchinski et al. 2000, 2001; Marcum et al. 2001; Windhorst et al. 2002; Papovich et al. 2003). The UV emission from galaxies is generally dominated by the light from young, massive stars, and as a result a galaxy's morphology at UV wavelengths can appear as a later–type system compared to that derived at optical wavelengths. The composition (ratio of the number of young to old stars) and configuration (heterogeneity in the distribution of young and old stars) of the stellar populations within elliptical, spiral, and irregular galaxies varies widely. Galaxy morphology can vary strongly from optical to UV wavelengths, and comparing the morphological properties of galaxies at UV wavelengths likely provides an incomplete evolutionary picture.

To compare the appearances between high–redshift and local galaxies, one requires observations at near–infrared (NIR) wavelengths, which probe rest–frame optical wavelengths for $z \gtrsim 1$ galaxies. Several recent studies have focused on the morphological properties of high–redshift galaxies in their rest–frame optical using *HST* high angular resolution NICMOS data (e.g. Teplitz et al. 1998; Dickinson 2000; Corbin et al. 2001; Moth & Elston 2002; Conselice et al. 2003; Stanford et al. 2004) and ground–based data (e.g. Labbé et al. 2003; Trujillo et al. 2004), and this was a strong motivation behind our NICMOS imaging survey of the HDF–N. This dataset combined with the *HST*/WFPC2 data (Williams et al. 1996) provides high angular resolution images ($\sim 0\farcs1$) in six bandpasses spanning $0.3-1.6$ μm, which permits comparisons between galaxy morphologies at rest–frame UV–optical wavelengths as a function of redshift for $0 < z \lesssim 3$.

In this paper, we investigate the distribution of the morphologies, sizes, colors, and internal colors of high–redshift galaxies ($z \sim 0.7-3.0$) in the HDF–N using data available from the *HST* datasets. In a previous paper (Papovich et al. 2003, hereafter P03), we presented a diagnostic to measure a galaxy's internal color dispersion, which quantifies the differences in galaxy morphology as a function of observed wavelength (i.e., it quantifies the morphological *K*–correction). Here, we apply this statistic to the rest–frame UV–optical colors of a sample of galaxies selected from the deep *HST*/NICMOS observations of the HDF–N. In § 2, we present a summary of the data and reduction procedures for the HDF–N data and define galaxy samples used here. In § 3, we describe the galaxy morphologies, and quantify their sizes, colors, and internal color dispersion. In § 4, we discuss differences in these quantities versus redshift, and compare these with simple scenarios of galaxy evolution. In § 5, we summarize our results. Throughout this work, we assume a cosmology with $\Omega_M = 0.3$, $\Lambda = 0.7$, and a Hubble parameter of $h = 0.7$ (where the present–day Hubble constant is $H_0 = 100\,h$ km s^{-1} Mpc^{-1}). All magnitudes have units in the AB system (Oke, Gunn, & Hoessel 1996), $m_{\rm AB} = 31.4 - 2.5\log(\langle f_\nu \rangle / 1\,{\rm nJy})$. We also refer to the four WFPC2 (F300W, F450W, F606W, F814W) and the two NICMOS (F110W, F160W) bandpasses used on the HDF–N as U_{300}, B_{450}, V_{606}, I_{814}, J_{110}, H_{160}, respectively.

2. THE DATA AND SAMPLE DEFINITION

The complete HDF–N was observed with NICMOS for GO proposal 7817 during the UT 1998 June NICMOS refocus campaign.[5] The details of the observations, data reduction, and object cataloging will be presented elsewhere (see also Dickinson et al. 2000; Papovich et al. 2001; Dickinson et al. 2003; Stanford et al. 2004). Briefly, we observed the complete *HST*/WFPC2 field of the HDF–N with eight sub–fields with the NICMOS Camera 3. Each sub–field was imaged three times through both the F110W and F160W filters, and each image was dithered into three separate exposures (resulting in nine independent, dithered positions in each sub–field), with a net exposure time of 12600s per filter. The data were processed using standard STScI pipeline routines and custom software, and combined into a single mosaic that was registered to the HDF–N WFPC2 images (Williams et al. 1996) using the "drizzling" method of Fructher & Hook (2002). The WFPC2 and J_{110} images were then convolved to match the H_{160} point–spread function (FWHM $\approx 0\farcs22$) in order to ensure that photometry was measured through similar apertures in each image. Our tests on point sources in the PSF–matched images indicate that photometry between bands is accurate to within 5% for aperture radii greater than $0\farcs1$. Object catalogs were constructed using SExtractor (Bertin & Arnouts 1996) by detecting objects in a combined $J_{110}+H_{160}$ image and measuring fluxes through matched apertures in all individual bands. As in Stanford et al. (2004), we will refer to the complete galaxy catalog as the HDF NICMOS Mosaic, or HNM, catalog. Relative photometry from the *HST* WFPC2 and NICMOS data was measured through matched elliptical apertures defined using the radial moments of each galaxies' F110W + F160W light profile (i.e., the SExtractor MAG_AUTO flux measurements). The difference between the flux measured in the total (MAG_AUTO) apertures and the isophotal (MAG_ISO) apertures has a median value of $\approx 6\%$ for all of the galaxies with $H_{160} \leq 25.5$.

In this work, we define two galaxy samples from the HDF–N data selected on the basis of redshift and limiting magnitude: a moderate–redshift sample, $0.7 \leq z \leq 1.4$ (with a mean redshift $z \simeq 1$); and a high–redshift sample, $1.9 \leq z \leq 3.0$ (with a mean redshift $z \simeq 2.3$). We have used the most complete collection of HDF-N spectroscopic redshifts known (see Dickinson et al. 2003; and references therein). For the remaining galaxies, we have used the photometric–redshift catalog of Budavári et al. (2000) for the HDF–N based on the combined WFPC2 and NICMOS data.

Because we analyze the two-dimensional galaxy appearances, we have selected galaxies on the basis of signal–to–noise ratio (S/N) down to a limiting isophotal level, which is more appropriate than a pure, flux–limited sample as galaxies of larger sizes have lower S/N for a fixed flux density. We also select the objects in the bandpass that approximately corresponds to the rest-frame *B*–band emission. We select all galaxies at $z \sim 1$ with $\mathrm{S/N}(J_{110}) \geq 20$ within a limiting isophote above $\mu(J_{110}) \leq 26.5$ mag arcsec^{-2}. Similarly, we select galaxies at $z \sim 2.3$ with $\mathrm{S/N}(H_{160}) \geq 20$ within a limiting isophote above $\mu(H_{160}) \leq 26.5$ mag arcsec^{-2}. Our tests have shown that these limits on object S/N within an isophotal aperture are reasonable for measuring galaxy morphological and structural parameters (see P03 and discussion below). These limits in S/N correspond to approximate magnitude limits measured within the elliptical apertures (i.e., the SExtractor MAG_AUTO) of $J_{110} \sim H_{160} \sim 25.5$. The final galaxy samples have 113 objects at $z \sim 1$ and 53 objects at $z \sim 2.3$ that satisfy these selection criteria in S/N and redshift. Of the samples, 69% of the $z \sim 1$ galaxies and 62% of the $z \sim 2.3$ galaxies have spectroscopic redshifts. In the following analysis, we also compare the properties of the galaxy samples down to a fixed absolute magnitude, $M(B) \leq -20.0$, where both samples are mostly complete (see Dickinson et al. 2003). This luminous sub–sample contains 41 objects at $z \sim 1$ and 46 objects at $z \sim 2.3$.

The redshift ranges used here were chosen to take advantage of two attributes of the data. The apparent galaxy size remains roughly constant for $0.7 \lesssim z \lesssim 3.0$ because the angular–diameter distance — the ratio of an object's physical size to its angular size — changes little ($< 18\%$) for the default cosmology: from 7.1 kpc arcsec^{-1} at $z = 0.7$ to 8.5 kpc arcsec^{-1} at $z \sim 1.6$ (this is generally true for any plausible cosmology). Thus, the *HST* images provide roughly constant angular resolution of ~ 1.5 kpc for all the galaxies in this dataset nearly independent of redshift. Note, however, that the co-moving volume contained in the redshift slice $1.9 \leq z \leq 3.0$ is 2.3 times than contained by $0.7 \leq z \leq 1.4$.

The other advantage comes from the fact that at these redshifts combinations of the WFPC2 and NICMOS bandpasses probe approximately the same wavelengths in the rest–frame, which allows us to minimize morphological *K*–corrections between the two samples. We broadly define two rest–frame wavelength regions: the mid–UV ($\sim 2400-3800$ Å), and optical ($\sim 4000-6000$ Å). For the $0.7 \leq z \leq 1.4$ galaxy sample, the mid-UV–, and optical–wavelength regions correspond to the V_{606} and J_{110} bandpasses, whereas at $1.9 \leq z \leq 3.0$ these rest–frame wavelength regions correspond to the I_{814} and H_{160} bandpasses. We note that using a single bandpass to track a specific rest–frame wavelength for a wide redshift interval does induce overlap in wavelength and redshift coverage due to the width and central wavelengths of the of the *HST* filter curves. For example, due to its large width, the centroid of the J_{110} filter samples $\lambda_0 \sim 4600-6500$ Å for $z \sim 0.7-1.4$, and $\lambda_0 \sim 2750-3800$ Å at $z \sim 1.9-3.0$. One could devise a method to interpolate the observed bandpasses to acquire the flux at a common wavelength. However, this would in principle hinder the analysis here, as one of the goals of this work is to contrast and compare the individual color features of galaxies for common rest–frame wavelengths. Interpolation between bands would only suppress any intrinsic signal. Therefore, we have opted to use the fixed bandpasses as approximate surrogates for the rest–frame colors. Furthermore, our tests on the UV–optical colors of local galaxies (P03) has shown that the internal color dispersion is most sensitive to changes due to the the heterogeneity of the stars that contribute to the flux redward and blueward of the Balmer and 4000Å breaks. For the galaxies considered here, these breaks are always confined between the chosen bandpasses.

[5] During the 1998 refocus campaign (*HST* Cycle 7N) the *HST* secondary was moved to the optimal focus for the NICMOS camera 3. This has not been done in cycles following the installation of the NICMOS Cooling System (NCS) during the *HST* servicing mission 3B. As a result, the image quality of the HDF–N mosaic is significantly improved over what is currently available with NICMOS post–NCS. For example, the PSF FWHM of the HDF-N mosaic, $\approx 0\farcs22$ in H_{160}, is approximately 60% smaller than that of similar observations of the Hubble Ultra–Deep Field (R. I. Thompson, private communication; see also Roye et al. 2003).

3. GALAXY MORPHOLOGICAL AND STRUCTURAL PROPERTIES

Figures 1 and 2 show images of the 28 most luminous galaxies (in the rest–frame *B*–band) in each of the $z \sim 1$ and $z \sim 2.3$ samples. These figures illustrate the morphologies of the brightest galaxy members of each sample. Although the galaxies in each sample span comparable rest–frame luminosities, $-20.5 \gtrsim M(B) \gtrsim -22$, their morphologies are distinctly different. Many of the galaxies at $z \sim 1$ have regular and symmetric morphologies, particularly in the rest-frame optical images, and are similar to "normal" Hubble–sequence galaxies. Our by–eye classification of the J_{110} morphologies finds that of the brightest $z \sim 1$ galaxies $\simeq 43\%$ (12/28) have elliptical, lenticular, or spheroidal morphologies (HNM 144, 789, 847, 886, 1014, 1091, 1031, 1214, 1356, 1418, 1453, 1523), $\simeq 43\%$ (12/28) have spiral or disk morphologies (HNM 214, 388, 448, 577, 779, 1120, 1168, 1213, 1240, 1348, 1488, 1525), and only $\simeq 14\%$ (4/28) have irregular or compact morphologies (HNM 333, 360, 909, 1316). Many of the objects show strong differences between their morphologies at UV and optical wavelengths (i.e., strong morphological *K*–corrections), which is particularly apparent in those galaxies with spiral and/or disk morphologies.

In contrast, the brightest galaxies at $z \sim 2.3$ have either irregular (HNM 552, 1357, 163, 1358, 813, 814, 1513, 109, 850, 758, 701, 502, 804) or compact morphologies (HNM 110 661, 843, 466, 274, 741, 62, 67, 1047, 1550, 503, 229, 272, 230, 1199). Unlike the galaxies at $z \sim 1$, there are no galaxies with disk–like or spiral–galaxy morphologies at $z \sim 2.3$: no galaxies show evidence for spiral arms or for being edge–on disk systems. This is broadly similar to the morphological descriptions of $z \sim 3$ galaxies based solely on rest–frame UV observations (Giavalisco et al. 1996; Lowenthal et al. 1997). The majority of the optically bright galaxies at $z \sim 2.3$ have similar morphologies in the $V_{606}-$ (rest–frame 1500 Å) and $H_{160}-$ (rest–frame 4400 Å), which is even more significant because this wavelength baseline is longer than that shown for the $z \sim 1$ sample in Figure 1. The lack of significant morphological *K*–correction combined with the fact that these galaxies have blue UV–optical colors (Dickinson et al. 2003) implies that recent star formation dominates the UV–optical morphologies, which we discuss in more detail below (see also the discussion in P03).

3.1. *The Galaxy Size–Luminosity Relationship*

The panels in figures 1 and 2 show the images of the $z \sim 1$ and 2.3 galaxies at the same physical scale (i.e., each panel is approximately 40 kpc $\times$ 40 kpc). Qualitatively, the typical galaxy size appears to increase from $z \sim 2.3$ to $z \sim 1$, with the most dramatic evolution in the rest–frame *B*–band images. In this section, we quantify this observed evolution in terms of the galaxy size–luminosity distribution.

We derived approximate absolute *B*–band magnitudes by interpolating the $V_{606}I_{814}J_{110}H_{160}$ photometry to measure the apparent magnitude at rest–frame 4400 Å and applying the distance moduli with the default cosmology for the observed redshift. We quantify galaxy sizes with the half–light radius $r_{1/2}$, which is defined as the radius of the aperture that encompasses 50% of the object's total flux as derived by the SExtractor software. Our tests using simulated data with noise properties similar to that of the HDF–N indicates that the SExtractor measurements of the half–light radius are accurate ($< 10\%$ rms) for $S/N > 20$, which is satisfied for the galaxy samples used here.

Figure 3 shows the distribution of the derived half–light radii for the HDF–N galaxies as a function of their absolute magnitudes at rest-frame 4400 Å. The upper envelope of rest–frame *B*–band luminosities is roughly the same at $z \sim 1$ and $z \sim 2.3$ (see also the discussion above; Dickinson et al. 2003). These luminosities are comparable to those of the largest present–day early–type spirals and ellipticals (de Vaucouleurs et al. 1991; Bender, Burnstein, & Faber 1992). Many galaxies in both samples have luminosities well in excess of the present–day characteristic "L^*",[6] although the majority of galaxies extend to fainter luminosities.

The average galaxy half–light radius grows with time from $z \sim 2.3$ to 1. The $z \sim 2.3$ galaxies have relatively small intrinsic sizes, $1 \lesssim r_{1/2} \lesssim 4$ kpc, with a mean value $\langle r_{1/2} \rangle \simeq 2.3 \pm 0.3$ kpc for $M(B) \leq -20.0$, where the error represents the uncertainty on the mean. In contrast, the measured radii of the $z \sim 1$ galaxies are larger for comparable absolute magnitudes. The mean half–light radius for galaxies with $M(B) \leq -20.0$ is $\langle r_{1/2} \rangle \simeq 3.2 \pm 0.3$ kpc, which is roughly 40% higher than the average size of the $z \sim 2.3$ galaxies. We find that based on the two–dimensional Kolmogoro–Smirnov (KS) test (Peacock 1983; Fasano & Franceschini 1987) the $z \sim 2.3$ and $z \sim 1$ galaxy samples, for $M(B) \leq M^*(B)$, trace different distributions at the $\simeq 99.96\%$ confidence level ($\simeq 3.6\sigma$). The luminosity–size distribution is qualitatively similar to results reported by Trujillo et al. (2004) for the HDF–S, but a quantitative comparison is beyond the scope of this work given the differences in rest–frame bandpass and sample redshifts.

In addition, there is a dramatic increase in the number density of large galaxies from $z \sim 2.3$ to 1. Considering only galaxies with $r_{1/2} > 3$ kpc and $M(B) \leq -20.0$, we find 24 galaxies at $z \sim 1$ and 8 at $z \sim 2.3$. Because the co-moving volume of the $z \sim 2.3$ redshift range is larger by a factor of 2.3, there is an increase in the number of large galaxies by a factor of ≈ 7 between these redshifts. Increasing the size limit to > 4 kpc makes the evolution even more dramatic: there are 13 such galaxies at $z \sim 1$ compared with only 2 at $z \sim 2.3$, but this comparison suffers from obvious small–number statistics. Note that our magnitude limits are also conservative. If we include fainter sources (e.g., to $M(B) \leq -19$), then the observed change is even greater: the number density of sources with $r_{1/2} > 3$ kpc increases by a factor of ≈ 11 from $z \sim 2.3$ to $z \sim 1$, but at the fainter magnitudes the $z \sim 2.3$ sample probably suffers from some incompleteness.

Note that we made no attempt to remove the contribution of the image PSF from the measured half–light radii. The NIC3 F160W PSF has a small intrinsic half–light radius, $r_{1/2,\rm PSF} \simeq 0.15''$, which for these redshifts and default cosmology corresponds to $r_{1/2} \simeq 1.2-1.4$ kpc. The majority of objects have $r_{1/2} \gtrsim 2$ kpc, to which the PSF contributes $< 20\%$. However, the PSF dominates the extrinsic sizes for objects with $r_{1/2} \lesssim r_{1/2,\rm PSF}$. Because the PSF can only increase the measured half–light radii, its effects will tend to *decrease* the amount of intrinsic size evolution between $z \sim 2.3$ and $z \sim 1$. Therefore, if anything our result underestimates the intrinsic evolution.

There is a deficit of HDF–N galaxies at $0.7 \leq z \leq 1.4$ in the HDF–N with $r_{1/2} \gtrsim 8$ kpc. Although this result could be interesting for the evolution and growth of galaxies for $z \sim 0-1$, it likely stems from the fact that the HDF–N data probes a small volume. The present–day bivariate (radius–

[6] Norberg et al. 2002 find a present–day characteristic luminosity of $M(B)^* = -20.5$ [AB], after slight adjustments in cosmology and bandpass.

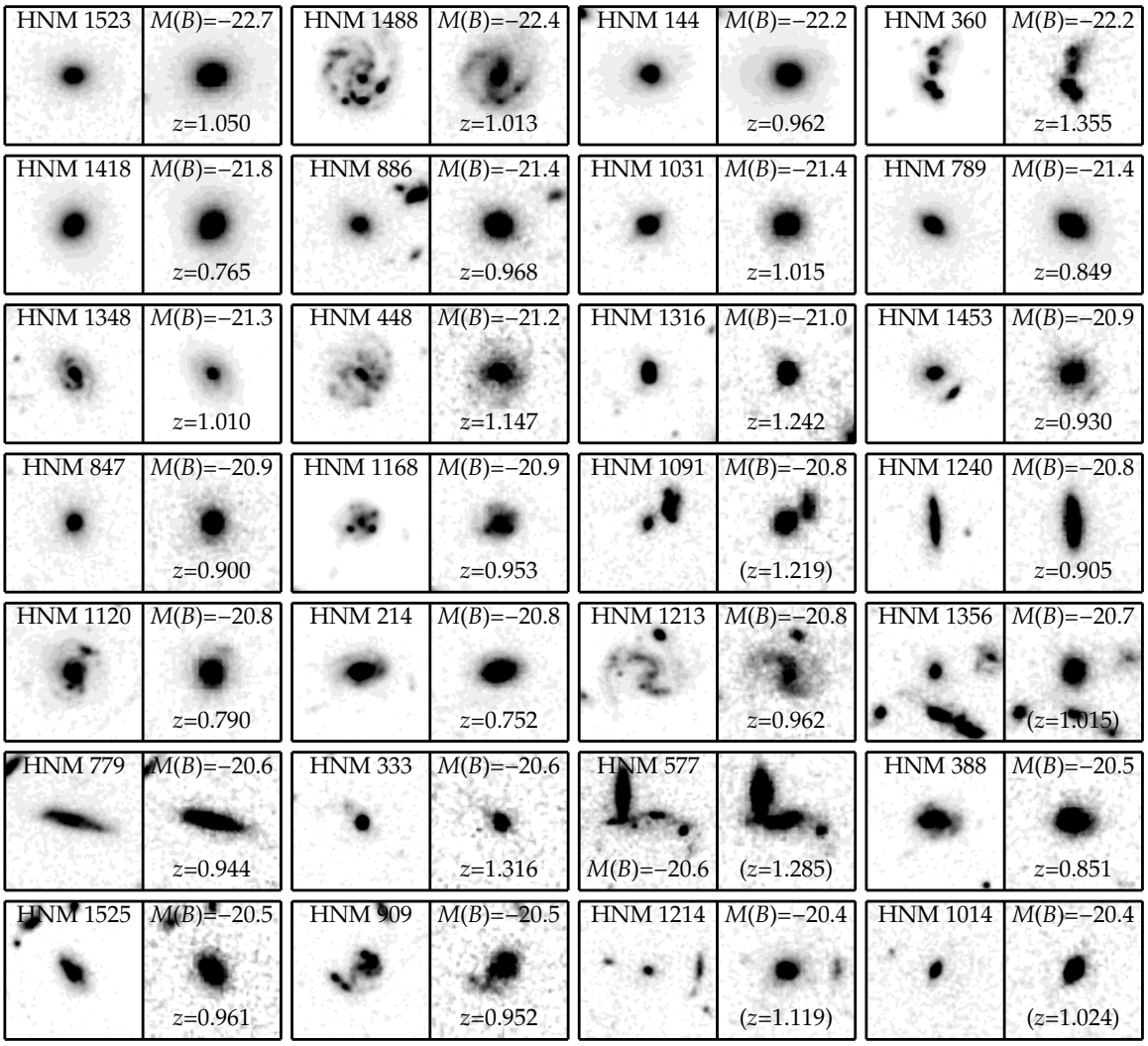

FIG. 1.— Rest–frame UV and optical images of 28 galaxies in the $0.7 \leq z \leq 1.4$ sample with the highest luminosities in the rest–frame *B*–band from the HDF-N. The left panel for each galaxy shows the WFPC2 F606W image, which corresponds to the rest–frame mid–UV wavelengths. The right panel shows the NICMOS F110W image, which depicts each galaxy approximately in the rest–frame *B*–band. Galaxies span luminosities $-22.7 \leq M(B) \leq -20.4$, and have redshifts as indicated in each image. Redshifts shown within parentheses indicate cases where only photometrically derived redshifts are available. Note the diversity in the galaxies appearances as a function of rest–frame wavelength. Each panel is 5×5 arcsec^2, which corresponds to $\simeq 40 \times 40$ kpc^2 in the rest–frame.

, luminosity–) distribution function (de Jong & Lacey 2000) predicts that there should be $\simeq 1.6 \pm 1.3$ objects with $r_{1/2} \geq 8$ kpc in the co–moving volume of the HDF–N for $0.7 \leq z \leq 1.4$. Therefore, the lack of galaxies with large radial sizes in the HDF–N at these redshifts is not strongly inconsistent with the present–day galaxy population: the volume is simply too small to expect many giant galaxies. This conclusion is reinforced by the presence of large galaxies in the disk–galaxy samples of Lilly et al. (1998), Simard et al. (1999), and Ravindranath et al. (2004) to $z \sim 0.7-1$, which are drawn from redshift surveys that cover larger solid angles. However, if the local galaxy size–luminosity distribution were applicable at higher redshifts, then one would expect to find $\simeq 5 \pm 2$ galaxies with $1.9 \leq z \leq 3.0$ and $r_{1/2} \geq 8$ kpc, and none are observed. Note that although Labbé et al. (2003) report several galaxies with $r_{1/2} \simeq 4-6$ kpc at $z \sim 2-3$ in the HDF–S, there are no candidates at these redshifts with larger radii.

The (rest–frame) *B*–band half–light radii of the $z \sim 2.3$ galaxies are consistent with those reported from $z \sim 3$ galaxies from observations solely in the rest–frame UV (Giavalisco et al. 1996; Lowenthal et al. 1997). This implies that UV–selected galaxies at these redshifts have high surface brightness at both rest–frame UV and optical wavelengths, and are not generally UV–bright star–forming regions within otherwise normal, larger host galaxies.

3.2. *Effects of Surface Brightness on Galaxy Sizes*

We have considered the effects of surface–brightness dimming, which rapidly increase with redshift (the bolometric surface brightness scales as $(1+z)^{-4}$). We simulated images of the luminous ($M(B) \leq -20.0$) galaxies from the $z \sim 1$ sample as they would appear at $z = 2.7$ (i.e., somewhat higher than the mean redshift $z = 2.3$ in order to achieve more conservative limits). The general details of this process are presented in P03, but briefly, we resampled the NICMOS J_{110} images of the $z \sim 1$ galaxies to the physical pixel scale for $z = 2.7$. We then appropriately reduced the pixel intensity to account for surface–brightness dimming and inserted them into blank regions in the NICMOS H_{160} images. Because the relative

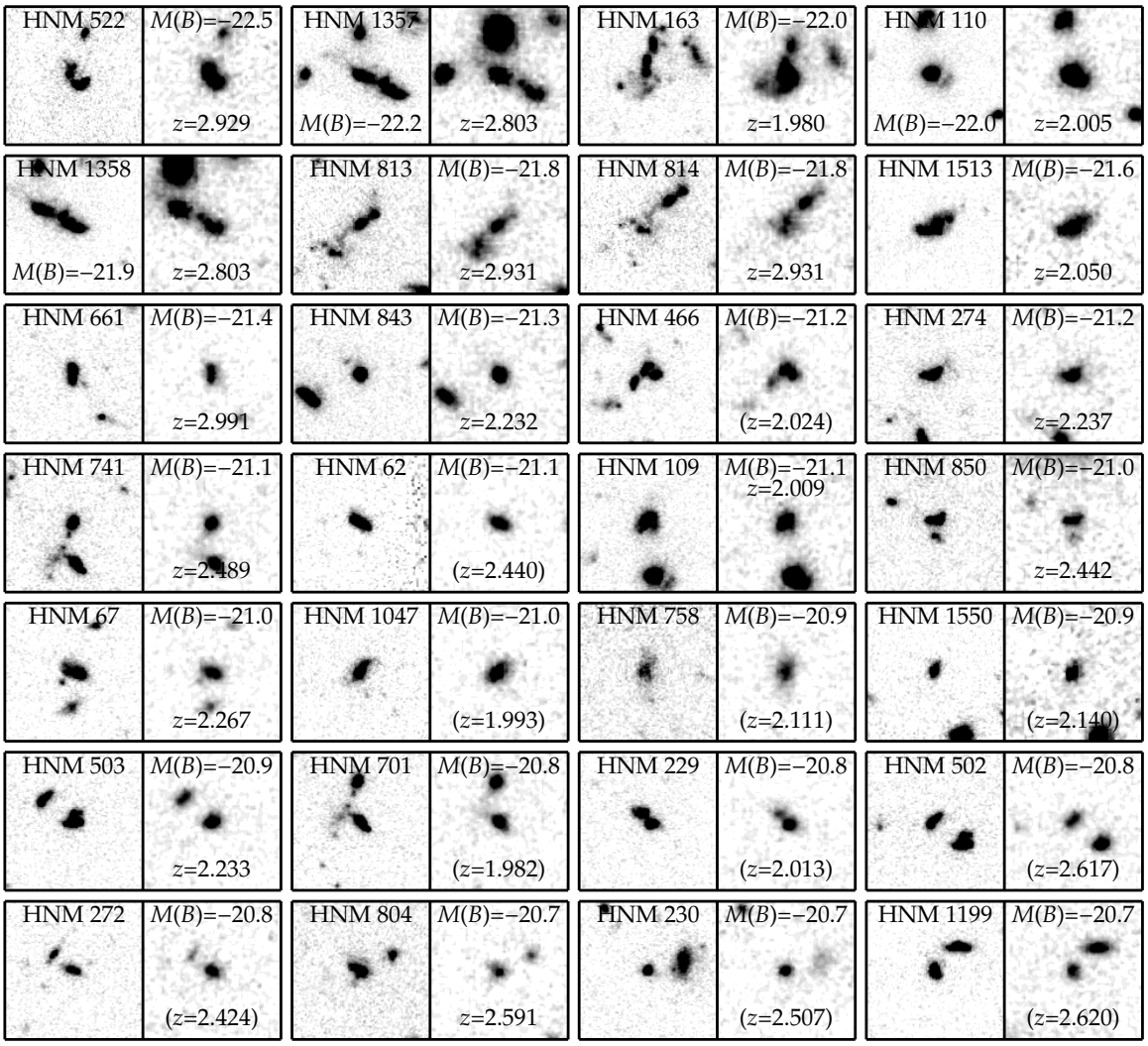

FIG. 2.— Same as Figure 1, but here the figure shows the 28 galaxies from the $1.9 \leq z \leq 3.3$ galaxy sample with the highest luminosities in rest–frame *B*–band. The left panel for each galaxy shows the WFPC2 F606W image, which corresponds to rest–frame far–UV wavelengths. The right panel shows the NICMOS F160W image, which corresponds approximately to the rest–frame *B*–band (i.e., the same rest–frame band as F110W for galaxies at $z \sim 1$). Note the lack of morphological transformation between wavelengths, even though these images span a longer wavelength baseline compared to Figure 1. The galaxies span luminosities $-22.5 \leq M(B) \leq -20.7$ (cf. to the similar range of galaxy *B*–band luminosities shown in Figure 1; see also Dickinson et al. 2003). The size of each panel is 5×5 arcsec^2, which corresponds to $\simeq 40 \times 40$ kpc^2 in the rest–frame.

resolution does not change substantially from $z = 0.7$ to 2.7, we have made the approximation that the image PSF does not vary in the simulated images. To compare these simulated $z = 2.7$ galaxies with the $z \sim 2.3$ HDF–N galaxy sample, we repeated the source detection and photometry processes using the SExtractor software to each simulated "redshifted" galaxy. The galaxy absolute magnitudes and characteristic radii were calculated on the simulated images in exactly the manner described previously.

Figure 4 shows the distribution of galaxy sizes with $M(B) \leq -20.0$ for the galaxy samples, and for the the $z \sim 1$ sample simulated at $z = 2.7$. The majority of the luminous $z \sim 1$ galaxies would be detected if they were present at $z \sim 2.7$. The mean half–light radius of the $z \sim 1$ galaxies simulated at $z = 2.7$ is reduced slightly: $\langle r_{1/2,\rm sim} \rangle \simeq 3.1$ kpc (reduced by $< 20\%$ compared to the results above). Using the one–dimensional KS–test to the half–light distributions of the $z \sim 2.3$ sample and the $z \sim 1$ sample simulated at $z = 2.7$, we find that these populations stem from different parent distributions at the 3.9σ level. Similarly, applying the two–dimensional KS–test to the subset of bright galaxies with $M(B) \leq -20$ (as done previously), the radius–luminosity distributions for the $z \sim 2.3$ galaxies and the $z \sim 1$ galaxies simulated at $z = 2.7$ trace different underlying distributions at the $\simeq 99.6\%$ confidence level ($\simeq 2.9\sigma$). Thus the strong size evolution that exists between galaxies at $z \sim 2.3$ and 1 is robust against surface–brightness dimming effects. This fact that the $1.9 \leq z \leq 3.0$ redshift range contains more co-moving volume than that at $0.7 \leq z \leq 1.4$ actually strengthens the significance of the result. For example, if we scale the number density of objects in each redshift interval to the same co-moving volume, then the one–dimensional KS–test derives a $> 5\sigma$ likelihood that the half–light distributions do not stem from the same parent sample.

3.3. *The Internal Color Dispersion of Galaxies*

In § 3.1 we describe the increase in the sizes of galaxies from $z \sim 2.3$ to 1. If galaxies grow monotonically in size, then

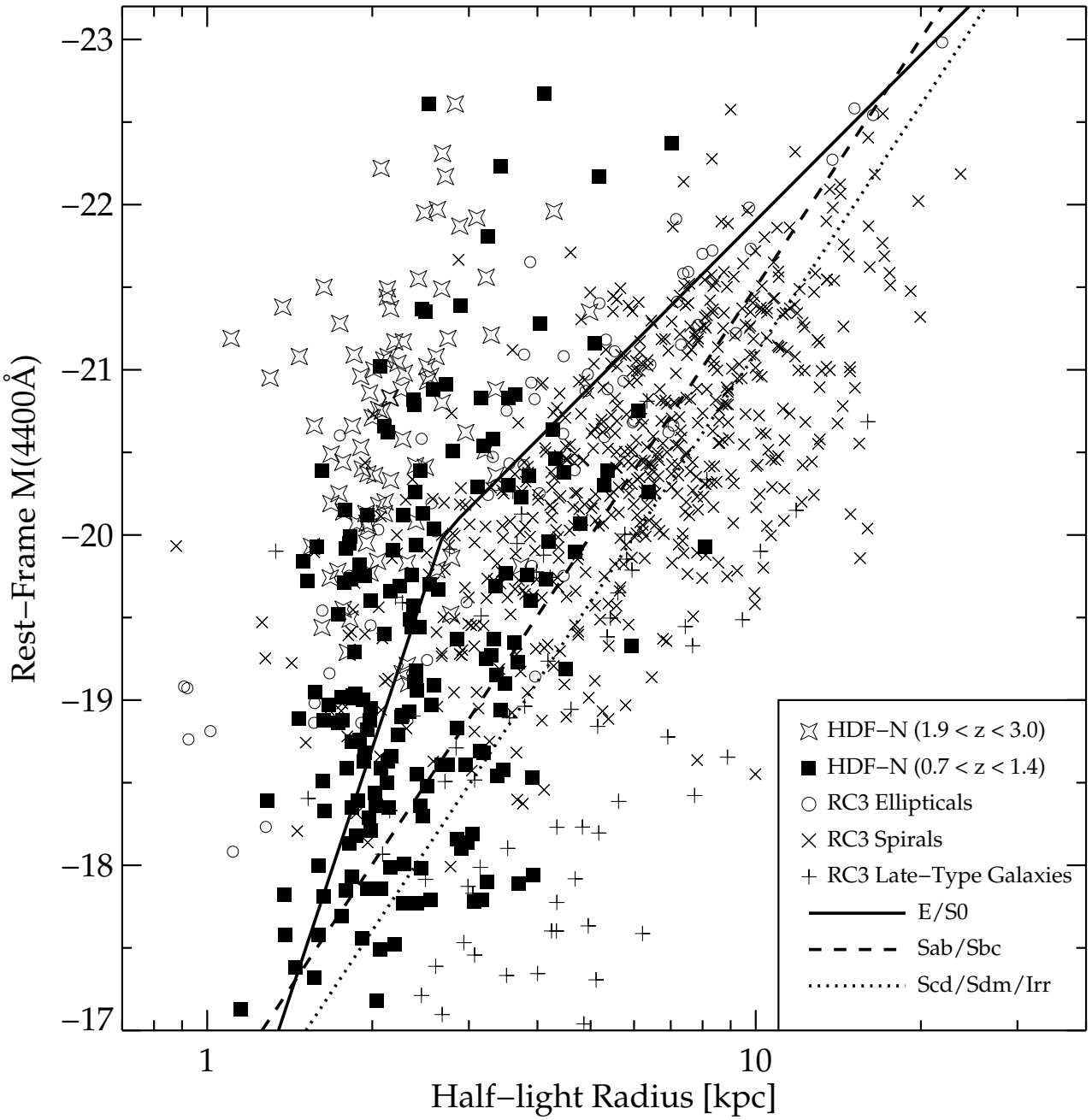

FIG. 3.— Distribution of galaxy half–light radii versus absolute magnitude in rest–frame light at 4400 Å. The absolute magnitudes are presented in AB units for the default cosmology. The plot shows the radius–luminosity distribution for the HDF–N $z \sim 2.3$ (open stars) and $z \sim 1$ (filled squares) galaxy samples, along with reference data collected from the RC3 catalog (de Vaucouleurs et al. 1991). The solid line indicates the relation for local E/S0 galaxies (Binggeli, Sandage, & Tarenghi 1984), and the dashed and dotted lines indicate the relation for local Sab/Sbc and Scd/Sdm/Irr galaxies, respectively (Freeman 1970; Roche et al. 1996). Note that the NICMOS F160W PSF corresponds to a half–light radius of $\simeq 1.2-1.4$ kpc for $z \sim 0.7-3.0$.

relatively young stars will form at larger radii at later times. An observable consequence of this growth may be that internal color structure develops within galaxies at later epochs.

To investigate possible internal color evolution in the HDF–N galaxy samples, we have quantified the galaxies' internal color dispersion between (rest–frame) UV–optical wavelengths of the HDF–N galaxies using the statistic defined in P03. The internal color dispersion quantifies the differences in galaxy morphology as a function of wavelength. In particular, the (rest–frame) UV–optical internal color dispersion characterizes diversification in the spatial configuration of young stellar populations (which dominate the rest-frame UV emission) and older stars, which contribute more to the optical light. In summary (see P03 for details), the internal color dispersion, ξ, is defined as the dispersion of the pixel intensities between two bandpasses about a mean color, normalized to

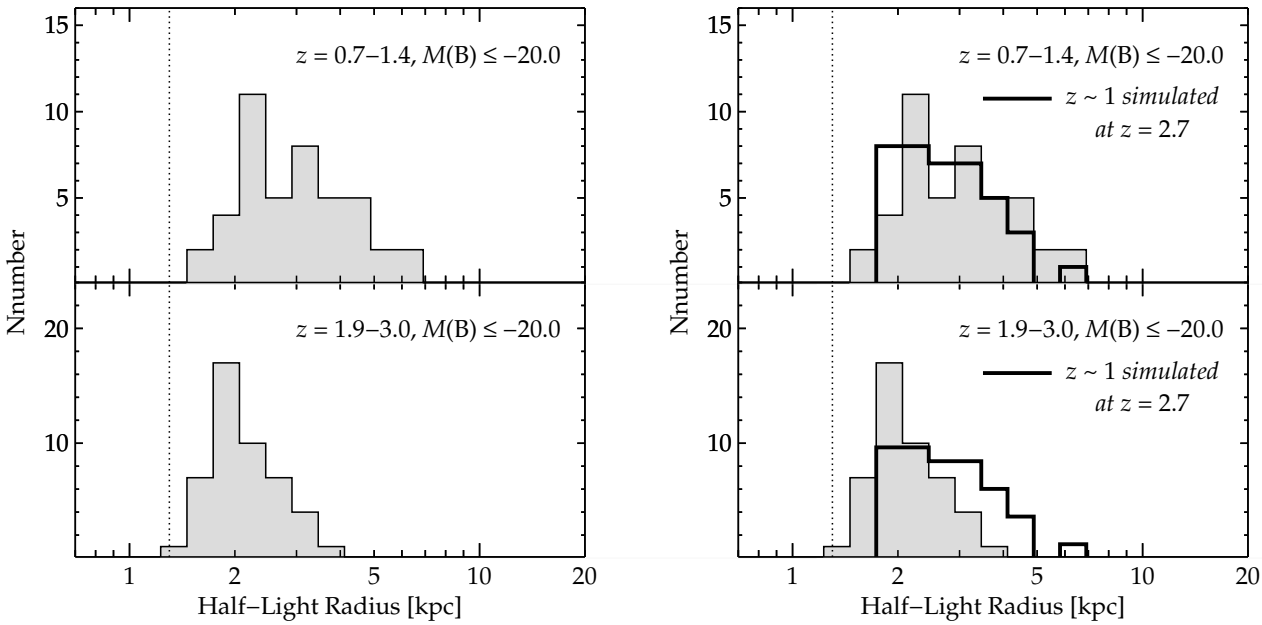

FIG. 4.— Distribution of galaxy sizes for the $z \sim 2.3$ and $z \sim 1$ HDF–N samples for objects with $M(B) \leq -20.0$. In both panels, the shaded histograms show the measured distributions. In the *right* panel, the thick, solid lines illustrate the observed distribution of the $z \sim 1$ galaxies as measured from their appearances when simulated at $z = 2.7$ (see text), and normalized to the total number of objects in the shaded histogram of each panel. Note that the redshift range, $1.9 \leq z \leq 3.0$, contains approximately $2.3\times$ the co-moving volume as $0.7 \leq z \leq 1.4$, and so the deficit of large galaxies at $z \sim 2.3$ has even greater significance than what is illustrated in the figure. In each panel, the dotted line indicates the half–light radius of the NICMOS PSF.

the total flux of the galaxy, i.e.,

$$\xi(I_1, I_2) = \frac{\sum(I_2 - \alpha I_1 - \beta)^2 - \sum(B_2 - \alpha B_1)^2}{\sum(I_2 - \beta)^2 - \sum(B_2 - \alpha B_1)^2}, \qquad (1)$$

where I_1 and I_2 are the pixel intensity values from each image obtained in two bandpasses. The scaling factor α is the flux ratio, or *color*, between the images, while the linear offset β adjusts (if necessary) for differences in the relative background levels of the two images. To account for internal color dispersion resulting purely from fluctuations in the sky background, we subtract the contribution from background regions (i.e., image sections with no detected sources) in each image B_1 and B_2, respectively. The internal color dispersion, ξ, is flux–independent, quantifies the morphological *K*–correction of a galaxy between the bandpasses I_1 and I_2, and has an analytically understood error distribution.

We have computed the internal UV–optical color dispersion for the galaxies in the HDF–N samples using the V_{606} and J_{110} images for the $z \sim 1$ sample and I_{814} and H_{160} images for the $z \sim 2.3$ sample. The *HST* images do not have a straightforward distribution of background pixel values due to the correlated pixels from the data–reduction process of "drizzling" the images, and due to the fact the the WFPC2 and NICMOS F110W images were convolved to match the PSF of the NICMOS F160W image. Both properties of the data will tend to suppress inter–pixel noise. Thus, it is necessary to test that the analytic uncertainties in the internal color dispersion given in P03 accurately describe the statistical errors for galaxies in the *HST* data. We repeatedly inserted artificial galaxies with known internal color dispersion into blank regions of the HDF–N images, and then computed the distribution of measured internal color dispersion values. The width of this distribution provides an estimate of the uncertainty on ξ. Indeed, our simulations indicated that the analytically derived error $\delta(\xi)$ had underestimated the intrinsic uncertainty. We subsequently rescaled the derived $\delta(\xi)$ values by factors that were empirically derived from the simulations, i.e., $\delta'(\xi) = C\,\delta(\xi)$, with $C = 5.98$ for $\xi(V_{606}, J_{110})$ and $C = 7.14$ for $\xi(I_{814}, H_{160})$. It should be noted that while the corrected errors provide a good estimate for the statistical errors arising from the background pixel–to–pixel noise, they likely still underestimate the real uncertainties as they neglect systematic effects arising from, e.g., inaccurate PSF matching, image registration, image calibration, etc. In particular, errors in PSF–matching will have a stronger effect on compact, and centrally peaked objects, and are probably the dominant error source for the brightest objects.

Figure 5 shows the distribution of internal UV–optical color dispersion as a function of redshift for the galaxies in the HDF–N samples. Large uncertainties on ξ are generally indicative of objects with low signal to noise in a particular bandpass. As a fiducial reference, we use the internal color dispersion values for two local galaxies observed in the same rest–frame bands, M81 (the early–type spiral galaxy with the highest internal color dispersion in the local P03 sample) and M74 (a "typical" mid–type spiral galaxy in the P03 sample). In Figure 5, we show the derived internal color dispersion for these two galaxies after convolving them with the NICMOS F160W PSF, and resampling them to the same physical pixel scale as the high–redshift HDF–N galaxies in the *HST* images. This illustrates the internal color dispersion in these fiducial local galaxies (with no evolution) relative to the high–redshift objects.

There is an evident increase in the upper envelope of internal color dispersion between $z \sim 2.3$ and 1. Formally, the mean and scatter increase by roughly a factor two from $z \sim 2.3$

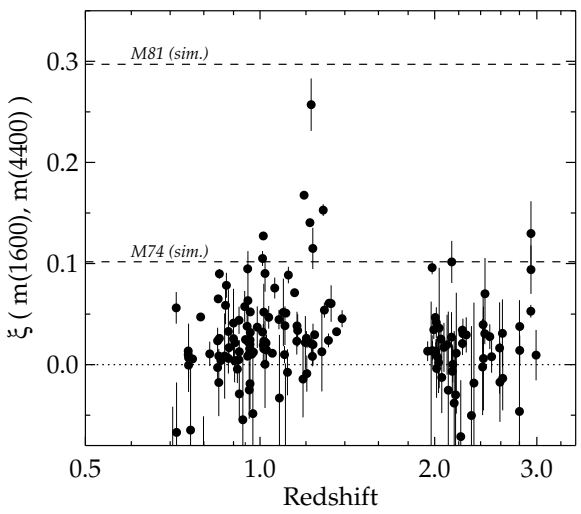

FIG. 5.— The internal color dispersion measured between the (rest–frame) UV–optical colors for the HDF–N galaxy samples as a function of redshift. The plot shows the internal dispersion: $\xi(V_{606},J_{110})$ and $\xi(I_{814},H_{160})$ for the $z\sim1$ and $z\sim2.3$ galaxies, respectively. Error bars indicate the approximate 1σ uncertainties (see text). The dashed lines in each panel show the derived internal color dispersion for two local galaxies (M81 and M74) after convolving with the NICMOS F160W PSF, and resampling to the same pixel scale as the high–redshift HDF–N galaxies.

to 1: from $\langle\xi(I_{814},H_{160})\rangle\simeq0.02$ at $z\sim2.3$ to $\langle\xi(V_{606},J_{110})\rangle\simeq0.04$ at $z\sim1$; and from $\sigma(\xi[I_{814},H_{160}])\simeq0.03$ at $z\sim2.3$ to $\sigma(\xi[I_{814},H_{160}])\simeq0.05$ at $z\sim1$. However, the change in the number of galaxies with large internal color dispersion is more dramatic. Most of the galaxies at $z\sim2.3$ have $\xi(I_{814},H_{160})\leq0.05$ (46/53), with a small tail to $\xi\sim0.1$ (7/53). In contrast, the $z\sim1$ sample contains many more objects with high internal–color dispersion — 28/113 (25%) of galaxies have $\xi(V_{606},J_{110})>0.05$ — including a sizable number (8/113) with values comparable to, or higher than, the mid–type spiral M74.

Note that it is unlikely that we are missing some significant fraction of galaxies at $z\sim2.3$ with high internal color dispersion. This is based on the facts that the $1.9\leq z\leq3.0$ redshift interval contains more than twice the co-moving volume as that of the $0.7\leq z\leq1.4$ (although cosmic variance uncertainties apply), the galaxies have been selected with the same limiting surface–brightness criteria, and the object resolution changes little for these redshifts (see § 2). Furthermore, in § 3.4 we argue that surface–brightness dimming effects are not responsible for the change in the internal color dispersion at these redshifts, which reinforces our results from P03 that the intrinsic rest–frame UV–optical internal color dispersion of local galaxies is recoverable for $0<z\lesssim3$. This evolution is not dominated by surface–brightness–dimming effects.

Figure 6 shows the galaxies with the highest $\xi(V_{606},J_{110})$ in the $z\sim1$ sample. Each object shows a significant qualitative difference between the rest–frame UV and optical images, which is quantified by the higher ξ values. Many of these galaxies have features indicative of early–to–late–type spiral galaxies (e.g., HNM 448, 860, 913, 1488, 1495), with a strong, central core in the J_{110} images, and prominent star–forming spiral arms in the V_{606} images with relatively bluer colors. These objects have internal color dispersion and color residual images qualitatively similar to that observed in local spirals, e.g., M81, M74, M100 (P03). Several of the $z\sim1$ galaxies in the figure show the appearance of inclined disk systems (e.g., HNM 577, 685, 1076, 1447), and the residual colors may suggest patchy dust and/or varied stellar content similar to nearby analogs; e.g., M82 and UGC 06697 (P03). There is also an actively star–forming galaxy with a disturbed morphology at all wavelengths and strong residual colors (HNM 909). This galaxy has a red core and blue outer regions, and it is possibly an spiral with some interacting activity, and a diverse stellar content and variable dust opacity. HNM 1453 shows clear multiple components of very different rest–frame UV–to–optical colors: a red elliptical galaxy with an off–center, blue component. This object has been identified as a gravitational lens candidate of a background object (see, e.g., Zepf, Moustakas, & Davis 1997). Thus, it seems that this object consists of two objects along the line of sight, which were not split in the HNM catalog. We will exclude this object from further analysis.

Figure 7 shows the galaxies in the $z\sim2.3$ sample with the highest $\xi(I_{814},H_{160})$ values. Nearly all the galaxies show evidence for disturbed morphologies, and the internal color dispersion probably arises from variations in the relative star–formation and variable dust obscuration. The exception is possibly HNM 163, which shows evidence for a redder core and a bright, off–center blue knot, and may result from variations in the stellar content. However, this galaxy has evidence for high dust obscuration (Papovich et al. 2001), which may also dominate the internal color dispersion.

Several pairs of the galaxies in $z\sim2.3$ sample have been "deblended" by the SExtractor software into two components: HNM 162 + 163; HNM 813 + 814; HNM 1357 + 1358 (see Figure 2). These galaxies all have spectroscopic redshifts, but the multiple galaxy components are merged at typical ground–based resolution ($\approx1''$), and as a consequence their spectra are blended as well. However, the photometric redshifts of the individual components (Budavári et al. 2000) are approximately identical in each case ($\delta z/(1+z)\lesssim0.02$). Although these individual components have similar redshifts (see Dickinson et al. 2003), it is unclear whether these objects actually are multiple components of the same parent galaxy or close galaxy pairs. In the analysis above we have kept the galaxies separated, but we have tested how merging them into single galaxies would affect the derived sizes and internal color dispersion. In three of the cases, the derived half–light radius increases by a factor less than two, with the exception being the case of HNM 162 + 163 where the half–light radius changes insignificantly. This would shift the galaxies in the radius–luminosity diagram (Figure 3), but would not alter any of the conclusions from that plot. In all four cases, the internal color dispersion of the merged pairs equals essentially the luminosity–weighted average of the internal color dispersion of the individual components. This has little effect on the distribution in Figure 5, and reduces the internal color dispersion of HNM 163 and 814, which have two of the largest values in the $z\sim2.3$ sample. Using the values for the merged objects would actually augment the change in the scatter of the internal color dispersion from $z\sim2.3$ to 1. We therefore keep the objects separated in order to be conservative in this evolution.

3.4. *Effects of Surface Brightness on the Internal Color Dispersion*

In this section we consider the effects from surface–brightness dimming on the internal color dispersion for in-

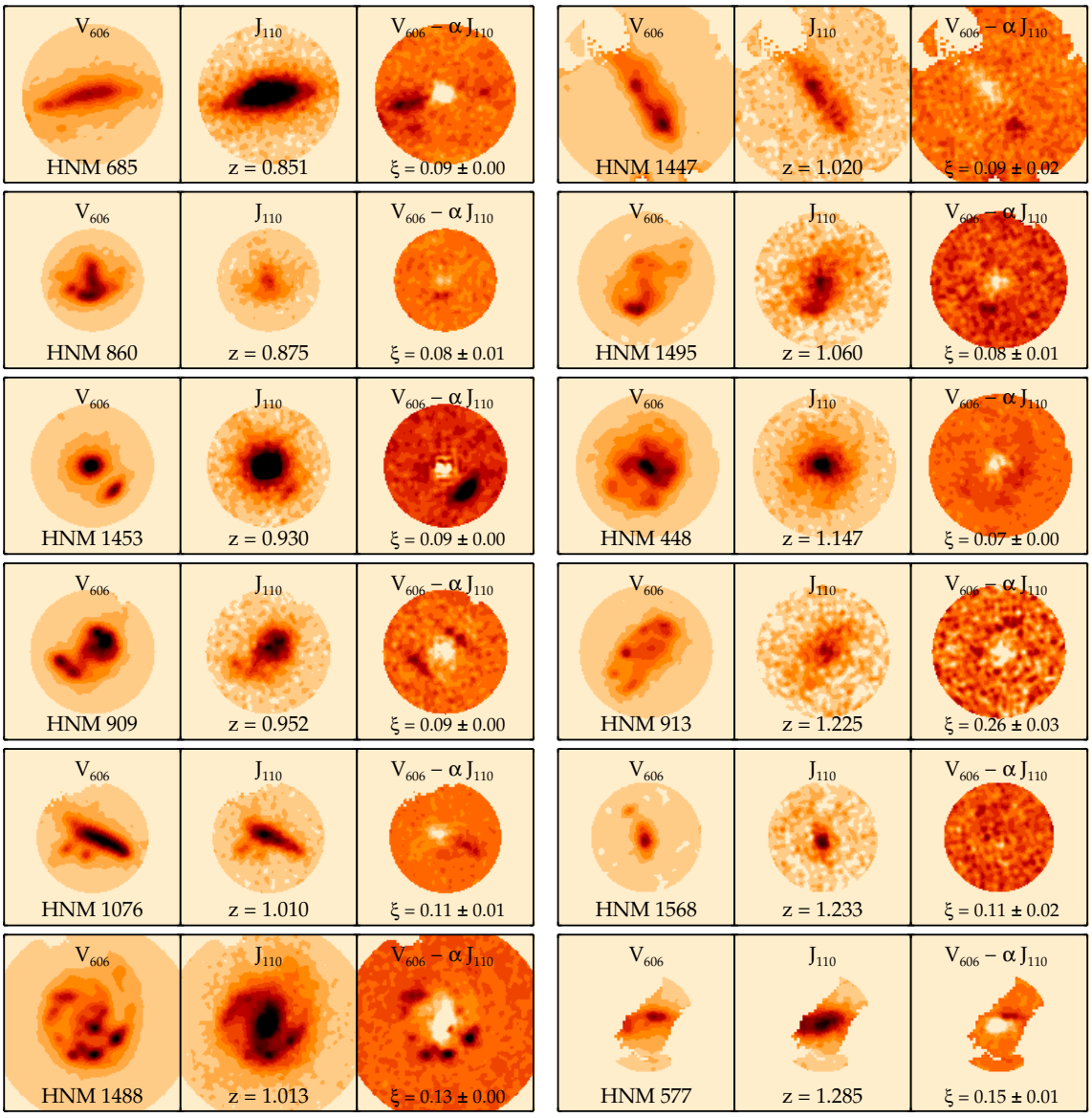

FIG. 6.— The internal color differences of the HDF–N galaxies with the highest $\xi(V_{606}, J_{110})$ values in the $z \sim 1$ sample. For each galaxy, the panels display the V_{606} and J_{110} images (as labeled); the right–most panel shows the difference between the images after scaling to remove the mean total color, i.e., these residuals show $I_1 - \alpha I_2 - \beta$, where I_1, and I_2 refer to the two images given in the panel inset as $\xi(I_1, I_2)$, and α and β are the fitted constants (see text for full description). The corresponding internal color dispersion value is shown in each color–residual image. Note that the color residuals are not the same as the definition of internal color dispersion (the latter is the squared sum of the former; divided by the squared sum of the image flux). Light/Dark regions correspond to features with internal colors that are redder/bluer than the mean total color. Each panel has dimensions of 5×5 arcsec^2, which corresponds to $\simeq 40 \times 40$ kpc^2 in the rest–frame for these galaxies.

creasing redshift. In P03, we tested this for local galaxies observed by *UIT*, and concluded that the internal color dispersion was fairly robust to $z \lesssim 3$ for galaxies with sufficient S/N in images with *HST*–like angular resolution. Here, we expand these tests by simulating the appearances of bright ($M(B) \leq -20.0$) galaxies in the $z \sim 1$ HDF–N sample. We simulated the appearance of each $z \sim 1$ galaxy at $z = 2.3$ (the median redshift of the high–redshift HDF–N sample) by appropriately resampling and dimming their images in the V_{606} and J_{110} bands, and adding noise from blank regions of the I_{814} and H_{160} images (see § 3.2, also P03). We then compute the internal color dispersion of these simulated galaxies using the procedures above.

Figure 8 compares the measured internal color dispersion of the $z \sim 1$ galaxies with the measured values from these galaxies simulated at $z = 2.3$ in I_{814} and H_{160} images. In general, the internal color dispersion values of the simulated high-redshift galaxies correlate with their measured values at $z \sim 1$. There is a slight reduction in the internal color dispersion values, which results from decreased signal–to–noise from cosmological surface brightness dimming.

Quantitatively, the number of galaxies with internal color dispersion values above the fiducial value $\xi \geq 0.05$ drops from roughly 35% at $z \sim 1$, to 26% for the simulated galaxies at $z = 2.3$. However, this is still significantly greater than the 15% of galaxies in the $z \sim 2.3$ sample with $M(B) \leq -20$ and $\xi \geq 0.05$. Furthermore, the reduction of the internal color dispersion in the simulated galaxies is possibly overestimated. In § 4.2, we argue that the I_{814}–H_{160} internal color dispersion at $z \sim 2.3$ is more sensitive to heterogeneities in a galaxy's

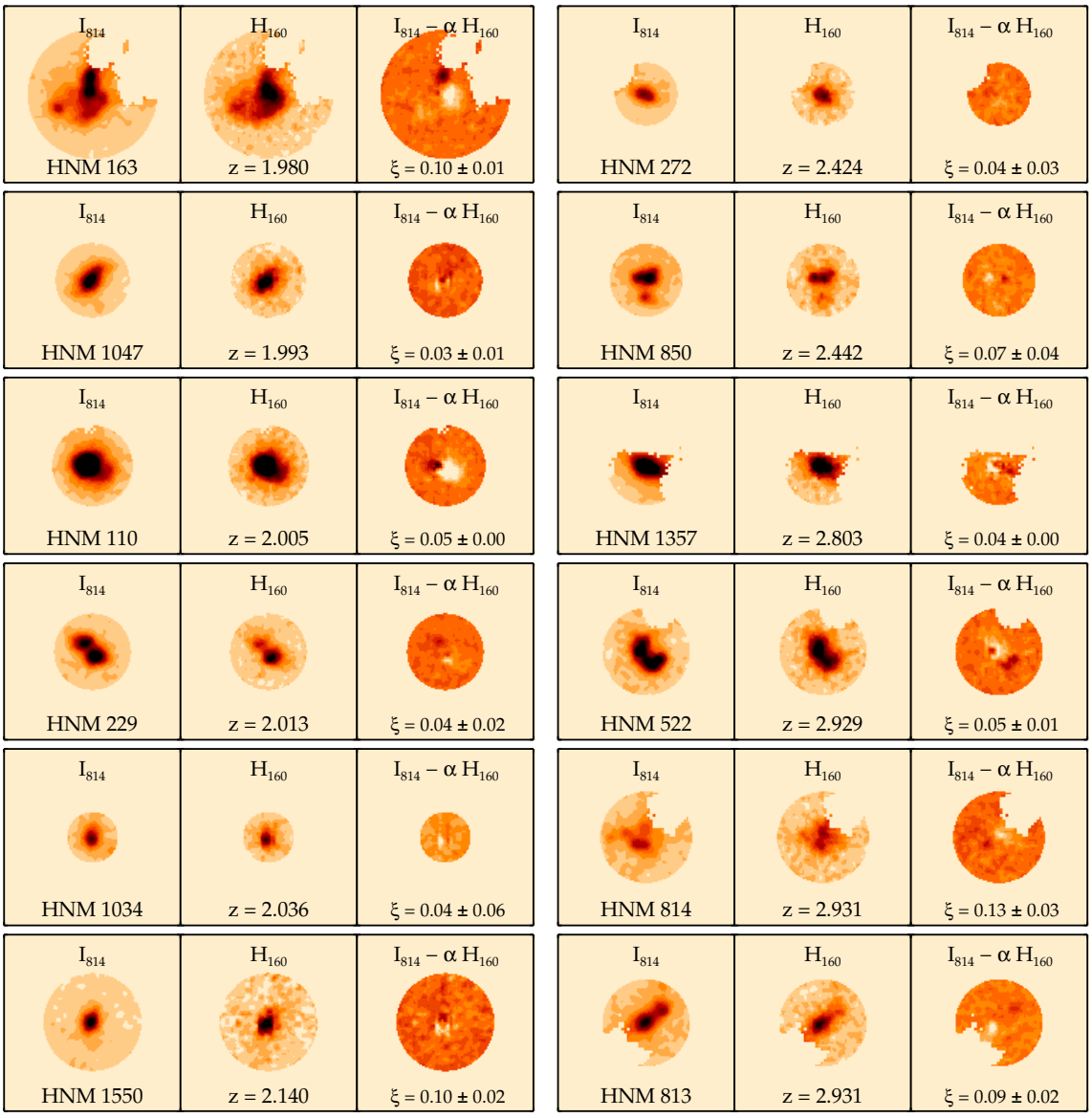

FIG. 7.— The internal color differences of the HDF–N galaxies with the highest $\xi(I_{814}, H_{160})$ values in the $z \sim 2.3$ sample. For each galaxy, the panels display the I_{814} and H_{160} images (as labeled); the right–most panel shows the difference between the images after scaling to remove the mean total color (see caption of fig 6). Each panel has dimensions of 5×5 arcsec^2, which corresponds to $\simeq 40 \times 40$ kpc^2 in the rest–frame for these galaxies.

stellar populations compared to the V_{606}–J_{110} internal color dispersion at $z \sim 1$. This is a consequence of the fact that at $z = 2.3$, the I_{814} bandpass probes rest–frame ≈ 2400 Å, while at $z \sim 1$, the V_{606} bandpass is sensitive to slightly redder rest-frame wavelengths, ~ 3000 Å. This is not taken into account in these simulations, and would increase the $\xi(I_{814}, H_{160})$ values of the simulated $z = 2.3$ galaxies by as much as $\sim 40\%$ (see § 4.2).

4. DISCUSSION

4.1. *The Growth of Galaxy Sizes*

The average size of luminous galaxies in the HDF–N between $z \sim 2.3$ and $z \sim 1$ increases by roughly a factor of $\simeq 1.4$. Characterizing this as a simple power–law with redshift, we find that the galaxy sizes evolve as $r_{1/2} \sim (1+z)^{-1.2 \pm 0.1}$ for $z \sim 1-2.3$. Hierarchical models predict that the characteristic sizes of galaxy halos grow as, $r_{\rm vir}(z) \propto M_{\rm vir}^{1/3} H(z)^{-2/3} \propto V_{\rm vir} H(z)^{-1}$ (e.g., Bouwens & Silk 2002; Ferguson et al. 2004). For the default cosmology, the Hubble constant evolves as $H(z) \sim (1+z)^{3/2}$, which implies that galaxy sizes should evolve roughly as $r_{vir} \sim (1+z)^{-(1-1.5)}$. Assuming the half–light radius scales as the virial radius, the observations here support this hierarchical picture of matter assembly within halos for $z \sim 1-2.3$. This result broadly agrees with predictions from other semi–analytical hierarchical models of galaxy formation (e.g., Baugh et al. 1998; Mo, Mao, & White 1999; Somerville, Primack, & Faber 2001).

The radius–luminosity distribution of $z \sim 1$ galaxies is roughly consistent with that of present–day galaxies and passive luminosity evolution. For example, for a monotonically evolving stellar population model (e.g., using the models of Bruzual & Charlot 2003) formed in a burst of star–formation at $z_f \sim 4$, one expects $\Delta M_B \simeq 1$ mag from $z = 1$ to $z = 0$. Thus, the data points for the $z \sim 1$ sample under this luminosity evolution would shift to regions of the $M_B - r_{1/2}$ distribution that

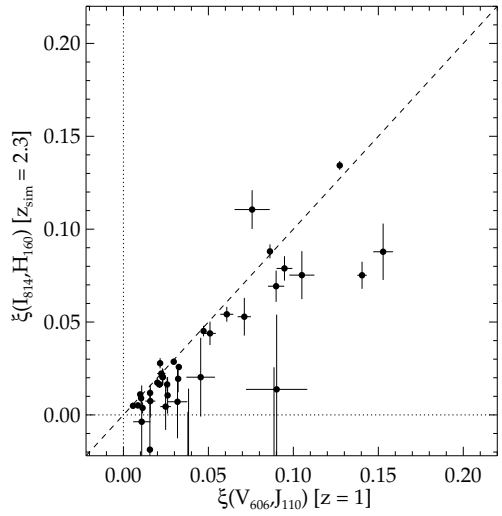

FIG. 8.— The effects of surface–brightness dimming on the internal color dispersion. The figure compares the internal color dispersion values of galaxies in the $z \sim 1$ sample with $M(B) \leq -20$, and the internal color dispersion of these galaxies simulated at $z = 2.3$. For each simulated galaxy, the I_{814} and H_{160} images were constructed by resampling their V_{606} and J_{110} images at a pixel scale corresponding to $z = 2.3$, and appropriately dimming their surface brightness. Note that the simulated $\xi(I_{814}, H_{160})$ may be *underestimated* because this color at this redshift is slightly more sensitive to heterogeneity in a galaxy's stellar populations compared with $\xi(V_{606}, J_{110})$ at $z \sim 1$, see § 4.2.

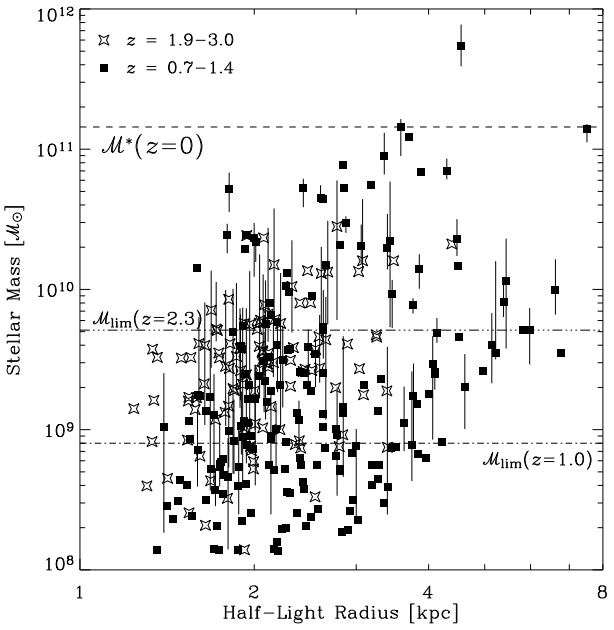

FIG. 9.— The galaxy size–stellar-mass distribution for the $z \sim 1$ and 2.3 samples from the HDF–N. Stellar mass estimates correspond to the derived values from Papovich et al. (2001) and Dickinson et al. (2003). Error bars on the stellar masses are shown for one–third of the objects to illustrate characteristic uncertainties. The dashed horizontal line shows the stellar mass of a present–day $\mathcal{M}^*$-galaxy (see, Cole et al. 2001, with adjustments to the default cosmology). The triple–dot–dashed and dot-dashed lines show the limiting stellar–mass for a maximally old object observed at the (10σ) flux limit of the data at $z = 2.3$ and 1, respectively. The data are sensitive to all sources with masses greater than these lines. Objects below these lines have lower mass-to-light ratios than the maximal model and are readily detected, but the completeness below these lines is less secure.

are occupied by local galaxies. However, it seems unavoidable that the progenitors of the largest galaxies in the $z \sim 1$ sample and at $z \sim 0$ are not consistent with simple luminosity evolution. Pure luminosity evolution would fade the $z \sim 2.3$ galaxies down the luminosity axis of Figure 3, where they have sizes that are too small compared with the observed distribution of galaxy sizes at $z \sim 1$. This result does not suffer from a selection bias in the sense that if the fully formed precursors to the $z \sim 1$ galaxies were already in place at $z = 2.3$, they would be observed in the deep NICMOS data (see § 3.2). Therefore, the $z \sim 2.3$ population are not the fully–formed predecessors of the $z \sim 1$ galaxies.

An alternative indication of growth for galaxies from $z \sim 2.3$ to 1 is evident from their radius–stellar-mass distribution, which is shown in Figure 9. Galaxy stellar masses have been estimated by fitting a suite of stellar–population synthesis models to the full spectrophotometry of the HDF–N galaxies (see Papovich et al. 2001; Dickinson et al. 2003). The stellar mass of a galaxy generally only increases with time (in the absence of interactions or tidal stripping that could eject stellar material),[7] which implies that evolution in a galaxies' stellar population manifests itself only in the positive direction of the ordinate in Figure 9. Galaxy–size evolution depends on the assembly history. Hierarchical models predict that the characteristic galaxy sizes scale roughly proportional to cosmic time (e.g., Bouwens & Silk 2002) from the accretion of surrounding material. This implies evolution in the positive direction along the abscissa in Figure 9 by a roughly factor of 1.5 from $z \sim 2.3$ to 1. However, the final half–*mass* size depends on the ratios of the sizes and masses of the progenitors. For example, using the relations presented in Cole et al. (2000) the radius of the merger product from two near–equal mass progenitors with size ratios, $R_2/R_1 = (1/3, 1, 3)$, is $R \simeq (0.7, 1.3, 2.2) \times R_1$, respectively. Note that in the case of $R_2/R_1 = 1/3$ that the final size is *decreased* relative to the size of the largest progenitor. Therefore, in the case of major mergers evolution in either direction along the abscissa of the figure is possible. As illustrated in Figure 9, the distribution of $z \sim 1$ galaxies extends to both larger stellar masses and sizes than galaxies at $z \sim 2.3$. The larger–stellar-mass galaxies ($\mathcal{M} \gtrsim 5 \times 10^{10}\ \mathcal{M}_\odot$) at $z \sim 1$ are not present in the $z \sim 2.3$ sample. At the same time, galaxies with larger half–light radii ($r_{1/2} \gtrsim 5$ kpc) appear at $z \sim 1$ in the HDF–N but not at higher redshifts. These galaxies in general have $M \lesssim 10^{10}\ \mathcal{M}_\odot$, similar to that found for the most massive galaxies at $z \sim 2.3$. The lack of larger galaxies with higher stellar masses at $z \sim 1$ is not unexpected simply because such objects are very rare and unlikely to be present within the volume of the HDF–N (see also § 4.1).

Previous studies of UV–bright $z \sim 3$ galaxies have concluded that their space density is roughly that of present–day, massive, early–type galaxies (Steidel et al. 1996; Giavalisco et al. 1998). Through arguments of the measured $z \sim 3$ clustering and angular separation, this population may trace a one–to–one correspondence with massive dark matter halos (Adelberger et al. 1998; Giavalisco & Dickinson 2001; Porciani & Giavalisco 2002). Because the cores of such mas-

[7] As stars evolve off the main sequence they eject a portion of their stellar mass back into the galaxies' gas reservoir. This amounts to a decrease in the total stellar mass of $\approx 30\%$ over the lifetime of a passively evolving stellar population.

sive halos will presumably evolve to become the locations of massive present–day galaxies, it is natural to equate this high–redshift galaxy population with that of present–day "L^*"–sized objects. One may expect galaxies in massive haloes to have an accelerated evolution, and thus they should assemble themselves at larger look-back times, which may partly be responsible for some of the observed evolution. This scenario is plausible, with the additional requirement that the galaxies necessarily undergo additional star formation and growth at $z \lesssim 2$ to match the $z \sim 1$ and present–day galaxy radius–luminosity and radius–stellar-mass distributions.

4.2. *The Distribution of Galaxy Colors from $z \sim 1-3$*

The scatter in the distribution of UV–optical total colors and internal color dispersion increases significantly in galaxies from $z \sim 2.3$ to 1. Figure 10 shows color–color plots and the internal color dispersion as a function of total color for the $z \sim 1$ and 2.3 galaxy samples. The figure also shows the colors from models of an evolving stellar population at $z = 1$ and 2.3 with three different monotonic star–formation histories (constant, instantaneous burst, and exponentially decaying) as a function of age from $10^7 - 10^{10}$ yr.

The $z \sim 2.3$ galaxies span a relatively small range of total color–color space even though they come from a IR–selected, flux–limited sample with complete photometric and spectroscopic redshift information (see § 2). The $z \sim 2.3$ galaxies have colors that are broadly consistent with those of a young, constantly star–forming stellar population with moderate amounts of dust reddening (see also Sawicki & Yee 1998; Papovich, Dickinson, & Ferguson 2001). Several objects have highly reddened rest-frame UV colors ($B_{450} - I_{814} \sim 1$; indicated by open symbols in the figure). All of these sources have redshifts $z \sim 2.9$ at which point the flux in the B_{450}-band is affected by Lyman α absorption from the IGM. This is not included in the model colors. Lyman α absorption does not affect the I_{814}–H_{160} internal color dispersion.

In contrast, the $z \sim 1$ galaxies show a greater scatter in their total colors. A significant fraction of the population has $U_{300} - V_{606}$ and $V_{606} - J_{110}$ colors that are well represented by stellar populations with declining star–formation histories, and ages greater than several gigayears. The $z \sim 1$ galaxies have colors spanned by the range of the models, including moderate dust extinction. Many of these objects have very red colors, $U_{300} - V_{606} \gtrsim 1.5$, $V_{606} - J_{110} \gtrsim 2$, and $S/N(U_{300}) < 10$, which implies their emission at UV–optical wavelengths is dominated by older stellar populations with little contribution from recent star formation. Several galaxies have rest-frame UV colors that are apparently inconsistent with the models (i.e., galaxies with $U_{300} - I_{814} \gtrsim 1.5$ and $V_{606} - J_{110} \lesssim 1$; indicated by open symbols in the plot). Two of these objects, HNM 748 and 1078, have spectroscopic redshifts $\simeq 0.9$, but photometric redshifts of 0.43 and 2.7, respectively. Thus the spectroscopic values (which were used to define the galaxy samples) are somewhat dubious. The other object, HNM 1141, has a photometric redshift with maximum likelihood at $z_{ph} = 1.2$, but with a poor goodness of fit. There is a second maximum near $z_{ph} \sim 3$ that has a nearly–equal likelihood. Given their redshift ambiguities, we will exclude these objects in subsequent analysis.

There is no clear correlation between total UV–optical color and internal color dispersion. While the $\xi(I_{814}, H_{160})$ values of the $z \sim 2.3$ galaxies are generally low, the galaxies with highest internal color dispersion ($\xi \gtrsim 0.05$) have the reddest total UV–optical colors ($I_{814} - H_{160} \gtrsim 1$ and $B_{450} - I_{814} \gtrsim 0.5$). This suggests that the red colors are due to either a mix of the stellar populations and/or variations in dust attenuation in the galaxies. At $z \sim 1$, many of the objects with high internal color dispersion have moderate rest–frame UV–optical colors, $V_{606} - J_{110} \sim 1$. This is similar to the trend between the internal color dispersion and UV–optical color in local galaxies (see P03, their figure 5), and suggests that high internal color dispersion results from a heterogeneous mix of young and old stellar populations (which produce the moderate total UV–optical colors) that are spatially segregated within the galaxies. The increase in the internal color dispersion for the galaxies in the $z \sim 1$ HDF–N sample — as well as the increased scatter in total colors of the galaxy population — implies that the $z \sim 1$ galaxy population has more diversity in its stellar populations compared to $z \sim 2.3$. We interpret this as evidence for old stellar populations that are not prominent at $z \gtrsim 2$.

Previous authors have studied the spatially resolved colors and color gradients of distant galaxies in order to interpret the star–formation histories of the stellar populations in these objects (e.g., Abraham et al. 1999; Corbin et al. 2001; Menanteau et al. 2001, 2004; Moth & Elston 2002). These studies have generally concluded that the spatial colors within galaxies reflect the evolutionary histories and internal dynamics of the galaxies' stellar populations. Abraham et al. (1999) and Menanteau et al. (2001, 2004) argued that the internal UV–optical colors are more sensitive to the relative ages of the galactic stellar populations than either dust or metallicity effects, and homogeneity in an object's internal color distribution is indicative of a broadly co-eval history for the galaxy's stellar populations. We reach a similar conclusion in our analysis of the local galaxy sample (P03). A more diverse star–formation history for a galaxy's stellar populations produces heterogeneous internal colors. For example, by investigating the internal colors of high–redshift ($z \lesssim 1$) galaxies in *HST* images, both Abraham et al. (1999) and Menanteau et al. (2001) find a large fraction ($\gtrsim 30-40\%$) of early–type galaxies in the field that show evidence for recent star formation activity.

Clearly, galaxies with very strong internal color gradients and heterogeneities as studied by these authors would probably also have large internal color dispersion. A small amount of ongoing star formation in an already massive galaxy can dominate its UV flux emission and give rise to strong variations in a galaxy's internal colors, even though it may constitute a negligible total to the galactic stellar mass (e.g., the "frosting" scenario of young stars in elliptical and lenticular galaxies; see Trager et al. 2000). Our measure of the internal color dispersion has an advantage that it can quantify the amount of ongoing star forming relative to the previously formed populations (see discussion below).

4.3. *Simulations of Galaxy Internal Colors*

A fraction of the $z \sim 1$ galaxies in HDF–N have morphologies of early–to–mid-type spiral galaxies, and these objects exhibit the highest internal color dispersion (see figures 6). This agrees with trends between morphology and the internal color dispersion observed in local galaxies (P03).

In most hierarchical merging models, the growth of rotationally supported galaxy disks is expected as gas cools and accretes toward the center of the underlying dark–matter halos (e.g., Mo, Mao, & White 1998), and this is broadly supported by the evolution in galaxy sizes (see § 4.1). This process is expected to form star–forming disks

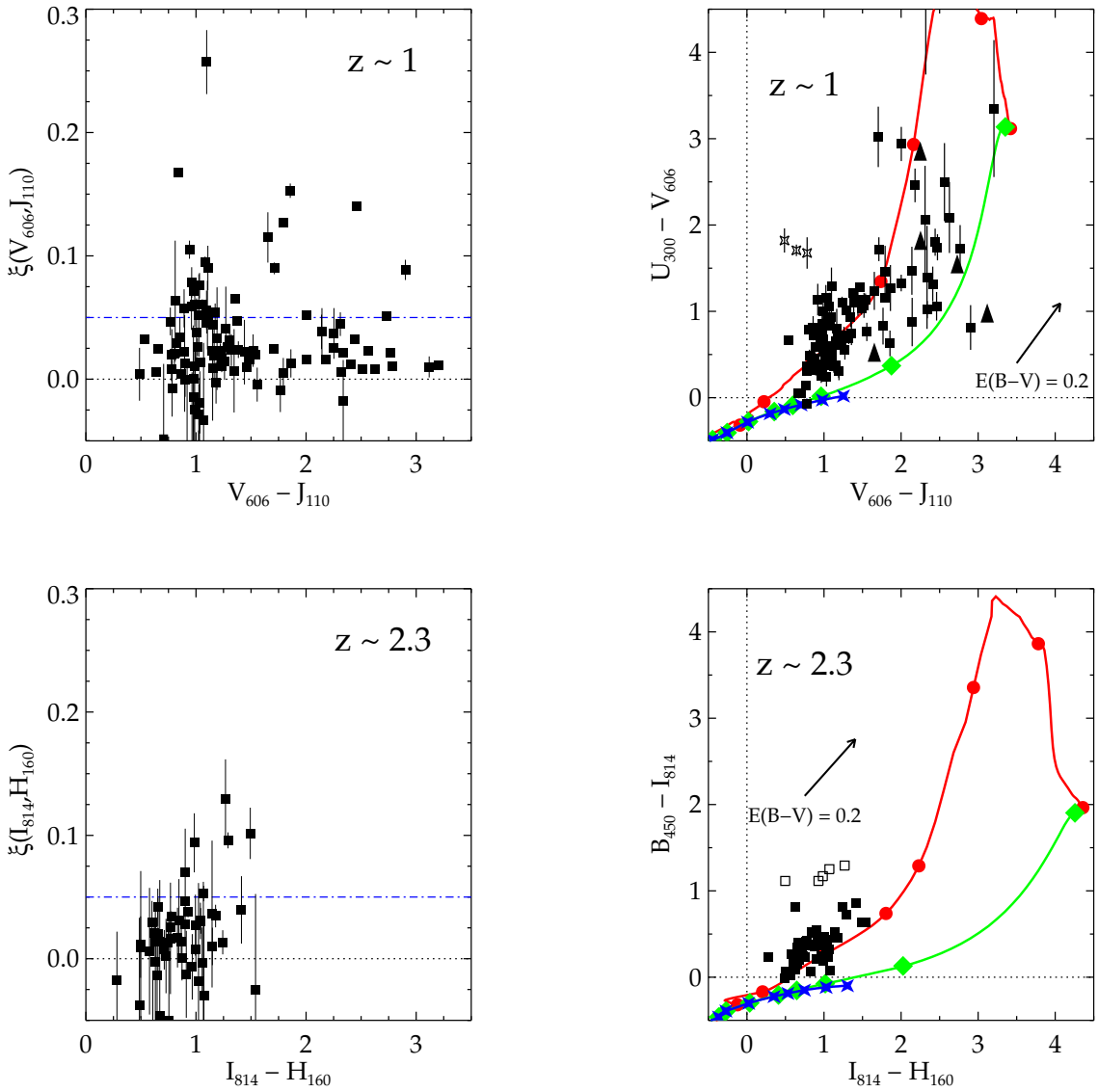

FIG. 10.— Distribution of galaxy internal color dispersion and total colors of galaxies at $z \sim 1$ (*top panels*) and $z \sim 2.3$ (*bottom panels*) in the HDF–N. The *left* panels show the derived internal color dispersion between the UV–optical bands as a function of the total UV–optical color. The blue, dashed horizontal lines indicate a fiducial value $\xi = 0.05$. The *right* panels show the (total) color–color plots for each galaxy sample. The open stars in the $z \sim 1$ plot correspond to objects with insecure redshifts (see text). The open boxes in the $z \sim 2.3$ plot correspond to objects with $z \sim 2.9$, where the B_{450}–band flux is attenuated by intergalactic Lyman α, which increases the observed $B_{450} - I_{814}$ color. In these plots, the three curves illustrate the colors in the observed frame for an evolving stellar population with three monotonic star–formation histories in the observed frame for $z = 1$ ($U_{300}V_{606}J_{110}$) and $z = 2.3$ ($B_{450}I_{814}H_{160}$) respectively. The blue curve with star symbols corresponds to a stellar population with a constant star formation rate. The green curve with triangle symbols corresponds to a stellar population with an exponentially decaying star–formation rate and e–folding time constant, $\tau = 1$ Gyr. The red curve with circles corresponds to a stellar population formed in an instantaneous burst. The symbols along each curve indicate the colors of the stellar population at an age of $\log(t/\mathrm{yr}) = 7, 8, 8.5, 8.7, 9, 9.5, 9.7, 10$. The arrows illustrate the reddening vector for a color excess, $E(B-V) = 0.2$, and assuming a starburst–like extinction law (Calzetti et al. 2000).

around spheroids produced in merger remnants, and create spiral galaxies, which broadly reproduces the observed distribution of colors, gradients, and masses in $z \sim 2$ – 3 galaxies (Contardo, Steinmetz, & Fritze-von Alvensleben 1998; Steinmetz & Navarro 2002).

To investigate how the formation of new disks around older spheroids affects the internal color dispersion, we considered a simple model to represent the galaxies at $z = 1$ and 2.3. We simulated galaxies with two components, an old spheroidal component and a young star–forming disk component, and assigned to these colors using the Bruzual & Charlot (2003) stellar population synthesis models and assuming a Salpeter IMF and solar metallicity (see Table 1). The spheroidal component was given the colors of a stellar population formed in an instantaneous burst viewed at an age of 2.8 Gyr and a $r^{1/4}$–law surface–brightness profile. The selected age corresponds to the maximum possible at $z = 2.3$, and approximately to the elapsed cosmic time between $z = 2.3$ and 1, and the half–light radius is consistent with the observed properties of the $z \sim 2.3$ galaxy sample and with the derived sizes of local galaxy bulges (Carollo 1999). The disk component has the colors of relatively young stellar populations (see Table 1), and an exponential surface–brightness profile. The disk brightness is incrementally increased relative to that of

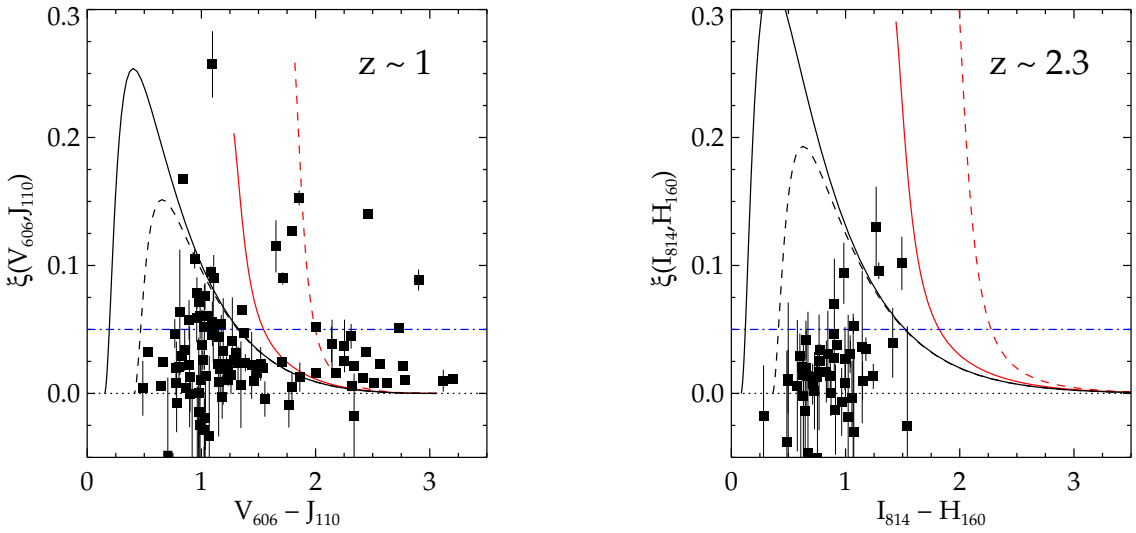

FIG. 11.— Distribution of galaxies internal color dispersion as a function of total UV–optical color. Data and symbols definitions are the same as in Figure 10. The curves in the correspond to the simple models discussed in the text. The black curves show the expected colors of galaxies with an old central bulge and star-forming exponential disk with different star–formation histories (model 1, dashed lines; model 2, solid lines; see text). The red curves illustrate the expected colors for objects with additional star-forming, H II regions within older, passively evolving stellar populations in a spheroid and disk (model 3).

the spheroid to span the full range of bulge-to-disk ratios.

The total colors and internal color dispersion of these models are plotted in Figure 11 with the data. Interestingly, the same model predicts larger $\xi(I_{814},H_{160})$ values at $z = 2.3$ relative to $\xi(V_{606},J_{110})$ at $z = 1$ by $\approx 40\%$. The $I_{814}-H_{160}$ color at $z = 2.3$ is bluer in the rest frame and covers a longer rest–frame wavelength baseline than the $V_{606}-J_{110}$ color at $z = 1$. Therefore, the $I_{814}-H_{160}$ is slightly more sensitive to the UV–optical color dispersion, and an object with the same intrinsic color dispersion would have a greater measured $\xi(I_{814},H_{160})$ at $z = 2.3$ than $\xi(V_{606},J_{110})$ at $z = 1$. This actually *strengthens* the conclusion that the range of the UV–optical internal color dispersion increases from $z \sim 2.3$ to 1.

The simple models of a star–forming disk surrounding an older central bulge span the range of total color and internal color dispersion observed in most of the galaxies at $z \sim 1$ that have moderate UV–optical colors. At low and high disk–to–bulge ratios, the model colors are nearly uniform (i.e., dominated by the disk and bulge respectively). The internal color dispersion is largest for mixed models. The stellar populations in these galaxies are consistent with this scenario.

However, there are many galaxies in the $z \sim 1$ sample with very red colors ($V_{606}-J_{110} \gtrsim 1.5$) and high internal color dispersion, and these are not accounted for by the simple models. The light from these objects must be dominated by relatively evolved stellar populations, possibly with small traces of ongoing star–formation to induce large internal UV–optical color dispersion (Trager, et al. 2000). To model this possibility, we considered the spheroid and disk models with an additional source of very young star-forming knots ("H II regions") typically located in galactic spiral arms and starbursts (described in Table 1). These models, plotted in Figure 11, reproduce the high internal color dispersion with redder total colors than the pure disk/bulge models. The high internal color dispersion is produced from spatially segregated and heterogeneous stellar populations. We therefore conclude that the increase in the internal color dispersion between $z \sim 2.3$ to 1 corresponds to greater diversity in the amounts of young and old stellar populations in these galaxies.

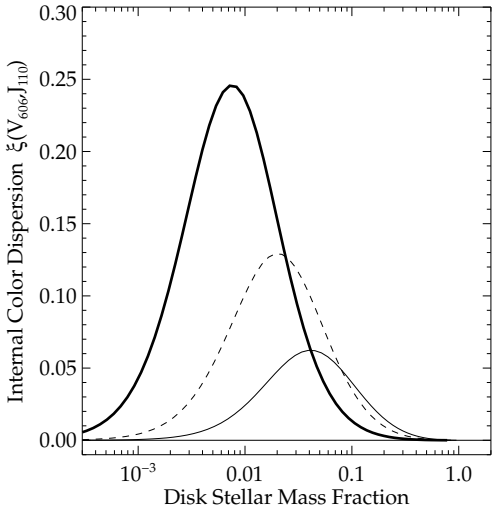

FIG. 12.— The measured internal UV–optical color dispersion from simulated galaxies as a function of the fraction of stellar mass in the young stellar populations of the disk, i.e., $\mathcal{M}_{\rm disk}/(\mathcal{M}_{\rm disk}+\mathcal{M}_{\rm bulge})$. The three curves correspond to galaxies with the spheroidal components and disk components listed in Table 1 (model 1, *dashed* line; model 2, *thick* line; model 3, *thin* line) viewed at $z = 1$.

The best example of this behavior in the $z \sim 1$ HDF–N sample is the giant, "grand–design" spiral galaxy, HNM 1488 (see figures 1 and 6). Bulge and possible bar features dominate the rest–frame *B*–band (J_{110} image). In the rest–frame UV (V_{606}), these features fade relative to the disk, spiral arms, and prominent star–forming knots embedded in the disk. The redder bulge dominates the rest-frame optical light, giving a red total color, $V_{606}-J_{110} = 1.8$. The internal color dispersion is very high, $\xi(V_{606},J_{110}) = 0.13$, and arises primarily from the

TABLE 1
GALAXY COMPONENT MODELS

Component (1)	t (2)	t/τ (3)	$r_{1/2}$ [kpc] (4)	Profile (5)	$\mathcal{M}/L_B$ $[\mathcal{M}_\odot/L_{B,\odot}]$ (6)	$V_{606}-J_{110}$ $z=1$ (7)	$I_{814}-H_{160}$ $z=2.3$ (8)
disk model 1	0.3 Gyr	0.6	7.5	Exponential	0.11	0.41	0.36
model 2	0.1 Gyr	1.0	7.5	Exponential	0.065	0.15	0.08
model 3	0.1 Gyr	4.0	7.5	Exponential	0.26	1.45	1.67
spheroid	2.8 Gyr	∞	2.3	de Vaucouleurs	2.7	3.06	4.83
H II region	50 Myr	≈ 0	···	Point source	0.032	–0.16	–0.27

NOTE. — (1) Galaxy component; (2) Age of stellar population; (3) Ratio of age to the star–formation rate e–folding timescale; (4) Half–light radius; (5) Profile; (6) Stellar mass to blue light ratio in solar units; observed frame colors at (7) $z = 1$, and (8) $z = 2.3$.

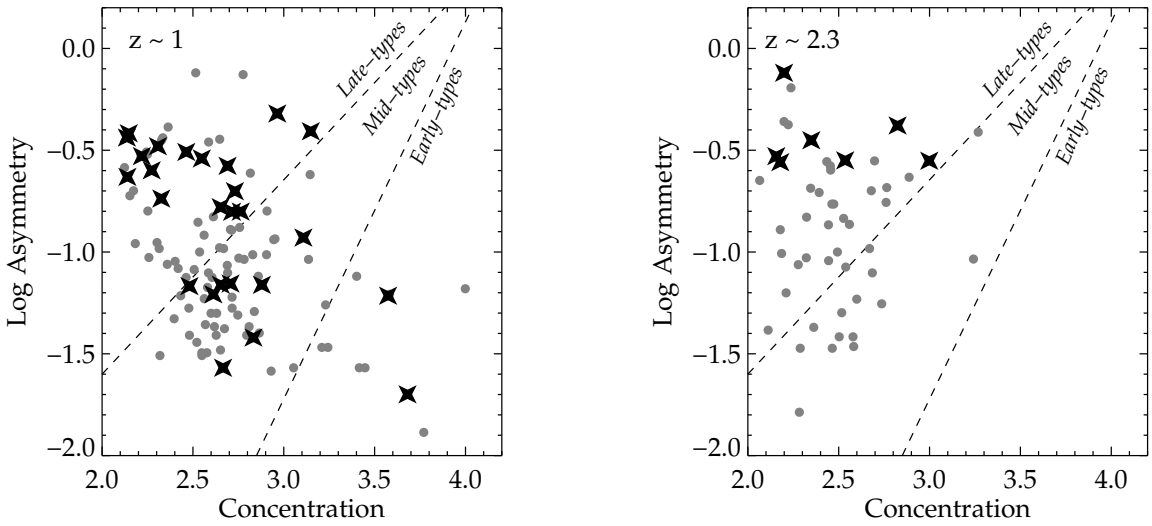

FIG. 13.— Distribution of concentration and asymmetry parameters of the $z \sim 1$ (*Left* panel) and $z \sim 2.3$ (*Right* panel) galaxy samples. Filled stars denote objects with $\xi(V_{606}, J_{110}) \geq 0.05$ and $\xi(I_{814}, H_{160}) \geq 0.05$ in the $z \sim 1$ and $z \sim 2.3$ panels, respectively. Objects with internal color dispersion values below this value are indicated by filled circles. The dashed lines denote rough fiducial regions in the *C–A* diagram that correspond to early (ellipticals, early–type spirals), middle (mid–type spirals), and late (irregulars and late–type spirals) Hubble–type galaxies (see Conselice et al. 2000).

color differences between the bulge, disk, and H II regions (Figure 6). Based on the models, these three features are required to produce both the red total color and high internal color dispersion.

The different galaxy components described in the simulations above have very different stellar-mass–to–blue-light ratios, as indicated in Table 1. Figure 12 shows the internal color dispersion of the models as a function of the relative amount of stellar mass in the different model components. For the disk models listed in Table 1, the stellar mass of the bulge exceeds that in the disk by up to a factor of $\sim 10-40$ when the luminosities of the bulge and disk are equal, and the internal color dispersion reaches a maximum near this point. Based on Figure 12, high values of the internal color dispersion ($\xi \gtrsim 0.05$) occur when $\lesssim 10\%$ of the stellar mass resides in recently formed stars (see also P03).

4.4. *Internal Color Dispersion as a Function of Morphology*

The increase in range of the UV–optical internal color dispersion coincides with the emergence of large, early– and mid–type Hubble–sequence galaxies. For example, Abraham et al. (1999) and Conselice et al. (2003) have shown that galaxy morphological type is generally distinguished by their concentration and asymmetry indexes (see also Conselice 2003). If the formation of Hubble–sequence galaxies corresponds to an increase in the scatter of the UV–optical color dispersion, then one expects there to be a relation between the internal color dispersion and these morphological indicators. Figure 13 shows the concentration and asymmetry values along with internal color dispersion for the two HDF–N samples (Conselice et al. 2003). At $z \sim 2.3$ galaxies with high UV–optical internal color dispersion occupy the upper range of asymmetry values, which is indicative of irregular star–forming galaxies possibly due to interactions and mergers (Conselice, Blackburne, & Papovich 2004a). This suggests that the internal color dispersion results from variations in the stellar populations and dust opacity, e.g., HNM 813 + 814 (see figures 2 and 7). Because galaxies with relatively high internal color dispersion correspond to highly asymmetric galaxies, this supports the notion that they are strongly interacting and/or merging. At $z \sim 1$ galaxies with high internal color dispersion span a range of morphological types as traced by concentration and asymmetry. There is still a group of galaxies with high internal color dispersion and high asymmetry. These objects are similar to the higher redshift star–forming galaxies, and is consistent with a recent analysis of

HST/ACS images, which suggests that star-forming galaxies at $z \sim 1.5$ and 4 have similar far–UV (1500 Å) morphologies (Lotz et al. 2005). There are also a large number of galaxies with low asymmetry, and higher concentration, which suggest that the high internal color dispersion in these objects occurs in otherwise normal mid/early–type galaxies. It seems that the emergence of Hubble–sequence galaxies coincides with larger internal color dispersion, and thus the assembly of diverse, spatially segregated stellar populations.

Two of the galaxies, HNM 1214 and 1453, are classified as early–types by high concentration and low asymmetry, and also have moderately high internal color dispersion ($\xi \simeq 0.08$). Upon visual inspection in both cases very faint blue companions are visible at distances of $\lesssim 1''$, which were not split by SExtractor and increase the internal color dispersion. The companion near HNM 1214 is visible roughly one arcsecond to the left of the galaxy in Figure 1. Companions only affect the internal color dispersion in very few of objects (these two and HNM 1453, which was eliminated from the sample for this reason, see § 3.3). The large internal color dispersion in the majority of objects results from spatially segregated heterogeneous stellar populations.

4.5. *Formation of Stellar Diversity in Galaxies from $z \sim 1-3$*

Many of the $z \sim 1$ galaxies have red total colors that are consistent with the passively evolving stellar–population models with ages older than $1-5$ Gyr. Because these ages are greater than the elapsed cosmic time from $z \sim 2.3$ to 1, some of the stellar populations currently in $z \sim 1$ galaxies must have been present in progenitors at the earlier epoch. However, due to the large growth in galaxy stellar mass and size over these redshifts, the $z \sim 1$ galaxies were generally not fully formed by $z \gtrsim 2$.

In addition to evolution in size and mass, the increase in the range of galaxy internal color dispersion from $z \sim 2.3$ to 1 is evidence that the diversity in the stellar populations in galaxies is increasing. Papovich et al. (2001) found that the relatively short ages of galaxies at $2 \lesssim z \lesssim 3.5$ (less than a few hundred megayears) coupled with the lack of older faded "post-burst" remnants implied that these galaxies have recurring star–formation episodes. The time scales of these episodes correspond to $\lesssim 1$ Gyr such that the newly–formed stellar populations dominate the rest–frame UV–optical wavelength regions of the galaxy SEDs. One cannot exclude the possibility that older (and possibly more heterogeneous) stellar populations are hidden beneath the "glare" of the young stars. This is broadly consistent with small range of low internal color dispersion observed in the $z \sim 2.3$ sample, but with the additional constraint that the nascent stellar populations in these galaxies dominate both the total galaxy colors and the internal galaxy colors, at least over scales of $\simeq 1.5$ kpc (the NICMOS resolution at these redshifts).

If either recurrent bursts such as those described above or quasi–constant star formation is the norm for galaxies at $z \sim 2.3$, then eventually these galaxies will form sufficient stellar mass, which will dominate the emitted optical luminosity. Strong UV–optical internal color dispersion generally requires that $\gtrsim 80\%$ of the total stellar mass resides in older stellar populations (see § 4.3). At $z = 2.3$, the age of the Universe is less than 3 Gyr, and thus there has been little opportunity for enough star–formation events to have instilled strong heterogeneity in the galaxies' stellar populations. At $z \sim 1$ the age of the Universe roughly doubles to ~ 6 Gyr, which permits a greater number of star–formation episodes with this timescale and allows for greater internal color dispersion. The increase in the internal color dispersion for $z \sim 2.3$ to 1 seems to require that enough time has elapsed for galaxies to have formed a sufficient amount of their stellar mass relative to their current star–formation rate such that the older stars dominate the optical luminosity.

The discussion above ignores the effects of dust extinction in star–forming regions, which can contribute to the overall "patchiness" in galaxy internal colors and produce strong morphological *K*–corrections (Windhorst et al. 2002). However, studies of the variation in internal colors (Abraham et al. 1999; Menanteau et al. 2004) and the internal color dispersion of local galaxies (P03) broadly conclude that these diagnostics are more sensitive to variations in the ages of the galaxy stellar populations relative to variable dust opacity. Therefore, we attribute the strong variation in galaxy internal color dispersion primarily to differences in the ages of the galaxy stellar populations.

Because the half–light radius is growing from $z \sim 2.3$ to 1 (see § 4.1), we know that galaxies do not form *in situ* and evolve passively over this redshift range. Furthermore, as the size increases, galaxies at later epochs will have proportionally more young stars at larger radii. So, size evolution will naturally lead to color gradients. This is supported by the fact that the $z \sim 1$ galaxies with the largest internal color dispersion appear to have red centrally concentrated cores with bluer regions at larger radii (see Figure 6).

Although the large internal color dispersion values at $z \sim 1$ imply a large stellar diversity at this epoch, the same is not the case at $z \sim 2.3$. Based on the simple models presented in § 4.3, although there is sufficient time at $z = 2.3$ for galaxies to have developed a heterogeneous stellar content with significant internal color dispersion, none is observed (see, for example, Figure 11). Therefore, we conclude that galaxies at $z \gtrsim 2$ are *not* forming a diverse stellar content as rapidly as is allowed purely from timescale arguments. This implies that galaxies at these epochs are not assembling their stellar populations in the quasi–continuous, inside-out models described in § 4.3.

One alternative to account for the fact that the $z \sim 2.3$ galaxies do not exhibit strong internal color dispersion is that intense, discrete starbursts such as those associated with actively merging galaxies dominate the star–formation histories at this epoch. Intense starbursts naturally dominate the UV–optical light at the time the galaxy is observed, which accounts for the observed properties of the galaxies at $z \sim 2-4$ (Lowenthal et al. 1997; Sawicki & Yee 1998; Steidel et al. 1999; Papovich, Dickinson, & Ferguson 2001; Papovich et al. 2004). Furthermore, if these starbursts arise from strong interactions or mergers, then during the merger one expects some internal color dispersion to result from any previously formed, heterogeneous stellar populations with some contribution from varying dust opacity (see, e.g., the large heterogeneity in both the stellar populations and dust extinction in NGC 4038/4039; Whitmore et al. 1999). The merger process will tend to erase any diversity in the constituent stellar–populations by fully mixing them on short timescales (e.g., Mihos & Hernquist 1996; Steinmetz & Navarro 2002), and thus the merger product should have largely homogenized stellar populations. This is consistent with the small derived values for the internal color dispersion at $z \sim 2.3$. The period while galaxies are strongly interacting and/or actively merging may produce patchy star formation with larger internal color dispersion. Indeed, the

objects at $z \sim 2.3$ with high internal color dispersion ($\xi \sim 0.05-0.1$) have large asymmetries (Figure 13), supporting the hypothesis that they are actively merging. We therefore interpret the observations as evidence for major mergers associated with strong starbursts. Furthermore, these events probably occur frequently, with the timescale between bursts $\lesssim 1$ Gyr, in order to keep the stellar content in these galaxies homogenized and to keep the total UV–optical colors dominated by the young starburst.

By $z \sim 1$ the internal color dispersion in galaxies has increased significantly, which we interpret as an increase in the diversity of galaxies' stellar content. This occurs partly because galaxies have formed sufficient mass in older stellar populations that recent star forming episodes contribute less to the total optical emission (while still dominating the UV light; see the discussion above). However, the heterogeneous stellar populations are spatially segregated: the $z \sim 1$ galaxies with the highest internal color dispersion typically have red central cores surrounded by bluer regions (see Figure 6). This signifies that major mergers occur less frequently, because any merger activity would tend to erase this diversity in the configuration of the stellar populations. The growth of large disks at this epoch naturally increases the internal color dispersion, and is consistent with the interpretation of the ubiquitousness of thick disks in local galaxies (Dalcanton & Bernstein 2002). Thus, the emergence of galaxies with large internal color dispersion signifies great diversity in their stellar content, and we interpret this as evidence for a decline in the major–merger rate in galaxies at $z \lesssim 1.5$ (see also van den Bergh et al. 2002; Conselice, Blackburne, & Papovich 2004a).

The decline in the importance of bursts with decreasing redshift may imply that more quiescent modes dominate the total star–formation rate. This is consistent with the suggestion by van den Bergh (2002) and reminiscent of the "collisional starburst" models of Somerville et al. (2001), where bursts dominate at high redshifts, and quiescent star formation dominates at lower redshifts ($z \lesssim 0.8$). The larger range of internal color dispersion for the massive galaxies at $z \sim 1$ implies that quiescent star–formation plays a more dominant role at later times compared to major mergers. The transition between where these modes dominate occurs between $z \sim 1.4-1.9$.

5. CONCLUSIONS

We have studied the evolution in the morphologies and colors of two samples of high–redshift galaxies at $z \sim 2.3$ and $z \sim 1$ in order to investigate how these galaxies assembled their stellar populations. From $z \sim 2.3$ to 1, galaxies grow in size, stellar mass, total color, and internal color dispersion, which we interpret as evidence for an increase in the diversity of stellar populations as galaxies assemble.

The majority of luminous galaxies ($M(B) \leq -20.5$ in the rest frame) in the $z \sim 1$ sample have rest–frame optical morphologies that are classifiable as early–to–mid Hubble types. These galaxies have regular, symmetric morphologies, and many show strong transformations between their morphologies when viewed at rest–frame UV and optical wavelengths. In contrast, the rest–frame optical morphologies of the luminous ($M(B) \leq 20.5$ in the rest–frame) galaxies at $z \sim 2.3$ are irregular and/or compact, and there is little difference in the galaxy morphologies from rest–frame far–UV to optical wavelengths. None of the $z \sim 2.3$ galaxies appear to be normal Hubble–sequence galaxies. Because the $z \sim 2.3$ galaxies show little transformation in morphology from rest–frame UV to optical wavelengths, the UV components are not generally the small, star–forming pieces within larger host galaxies.

The mean galaxy size increases from $z \sim 2.3$ to 1 by roughly 40%, in broad agreement with expectations from hierarchical models. Furthermore, the number density of large galaxies, $r_{1/2} > 3$ kpc and $M(B) \leq -20$, increases by a factor of ≈ 7. We have tested that the size evolution is robust against surface–brightness dimming effects. The half–light radii of the $z \sim 1$ galaxies when simulated at $z = 2.7$ decrease by $< 20\%$ compared to their measured values at $z \sim 1$, but this decrease is small compared to the observed evolution. The radius–luminosity distribution of galaxies at $z \sim 1$ is consistent with the local distribution for pure luminosity evolution. However, the size–luminosity, and size–mass distributions of $z \sim 2.3$ galaxies indicate that they are not the fully formed progenitors of large, present–day galaxies. Galaxies at $z \gtrsim 2$ must continue to build, both in terms of size and stellar mass.

We have analyzed the rest–frame UV–optical total colors, and the internal color dispersion using the novel statistic developed in P03. The internal color dispersion quantifies differences in galaxy morphology as a function of wavelength, and between rest–frame UV and optical wavelengths it constrains the amount of current star–formation relative to the older stellar populations. Both the mean and scatter of total color and the internal color dispersion increase from $z \sim 2.3$ to 1. At $z \sim 1$, galaxies with high internal color span a range of morphological types. Many are spiral galaxies, with a few starbursting and interacting systems. There is no clear correlation between total color and the internal color dispersion, although galaxies with the highest internal color dispersion have moderate total UV–optical colors, which implies a mix of heterogeneous stellar populations. The $z \sim 1$ galaxies with the highest internal color dispersion appear to be early–to–mid-type spiral galaxies, and they exhibit strong transformations between their UV and optical rest–frame morphologies. At $z \sim 2.3$ few galaxies have high internal color dispersion, and those that do also have interacting and disturbed morphologies, which implies that the UV–optical light from these galaxies is dominated by young, largely homogeneous stellar populations. We interpret the evolution in galaxy color and internal color dispersion as evidence that the diversity in the stellar populations of galaxies is increasing from $z \sim 2.3$ to 1 as the older stellar components build up over time.

To interpret the evolution in the properties of galaxies, we have modeled the stellar populations of galaxies in spheroidal and disk components, and star–forming H II regions. These simple models broadly support the conclusion that the range of internal color dispersion corresponds to increased diversity in the galaxies' stellar populations. Galaxies with significant bulge components with star–forming disks and/or compact, H II regions produce high internal color dispersion, and broadly reproduce the colors, sizes, and internal color dispersion of the high–redshift galaxies. We find that large values of the internal color dispersion require galaxy to have formed spatially segregated, diverse stellar populations where old stars dominate the optical light and stellar mass (i.e., $\gtrsim 80\%$ of the stellar mass resides in stars > 1 Gyr). For smaller fractions of old stars, young stellar populations dominate the UV–optical internal colors.

The scatter in the internal color dispersion of the $z \sim 2.3$ galaxies is smaller than what is allowed under these models and basic timescale arguments. We interpret this as evidence that brief, discrete and recurrent starburst episodes dominate the star–formation history of galaxies at this epoch. If these arise from strong interactions or mergers of gas–rich con-

stituents, then they will erase any heterogeneity in the stellar content that otherwise develops, and this is supported by the low internal color dispersion observed in galaxies at this epoch. The greater range of internal color dispersion that forms at $z \sim 1$ suggests that major mergers are less frequent and more quiescent star–formation mechanisms are the norm.

The greater diversity in the stellar populations of these high–redshift galaxies coincides with the emergence with large Hubble sequence galaxies. Large values of the UV–optical internal color dispersion require a diverse and spatially unmixed stellar population, and this occurs when galaxies have formed most of their stellar mass. In order to maintain the spatial heterogeneity between the young and old stellar populations also requires that major mergers are less common at this epoch. These conditions all occur at $z \lesssim 1.4$, which naturally allows galaxies with Hubble–sequence morphologies to develop.

We wish to thank our colleagues for stimulating conversations, the other members of the HDF–N NICMOS GO team who contributed to many aspects of this program, and the STScI staff for their optimal planning of the observations and efficient processing of the data. We are grateful to Tamás Budavári for helpful assistance and for providing the photometric redshifts, and to Eric Bell and George Rieke for their comments on this manuscript and many interesting discussions. We thank the anonymous referee for insightful and prompt comments, which improved the quality and clarity of the conclusions in this paper. We also wish to acknowledge the very generous hospitality and science–conducive environment of the Aspen Center for Physics, where much of this work was finished. CP also thanks STScI for hospitality on several visits while this research was completed. Partial support for this work was provided by NASA through grant GO-07817.01-96A from the Space Telescope Science Institute, which is operated by the Association of University for Research in Astronomy, Inc., under NASA contract NAS5-26555. CP acknowledges partial support by NASA through Contract Number 960785 issued by JPL/Caltech.

REFERENCES

Abraham, R. G., Ellis, R. S., Fabian, A. C., Tanvir, N. R., & Glazebrook, K. 1999, MNRAS, 303, 641
Abraham, R. G., Tanvir, N. R., Sanitago, B. X., Ellis, R. S., Glazebrook, K., & van den Bergh, S. 1996, MNRAS, 279, 47
Adelberger, K. L., Steidel, C. C., Giavalisco, M., Dickinson, M., Pettini, M., & Kellogg, M. 1998, ApJ, 505, 18
Baugh, C. M., Cole, S., Frenk, C. S., & Lacey, C. G. 1998, ApJ, 498, 504
Bell, E. F. et al. 2004, ApJ, 608, 752
Bender, R., Burnstein, D., & Faber, S. M 1992, ApJ, 399, 462
Bertin, E., & Arnouts, S. 1996, A&AS, 117, 393
Binggeli, B., Sandage, A., & Tarenghi, M. 1984, AJ, 89, 64
Bouwens, R. & Silk, J. 2002, ApJ, 568, 522
Brinchmann, J. et al. 1998, ApJ, 499, 112
Brinchmann, J., & Ellis, R. S. 2000, ApJ, 536, L77
Bruzual, G. A., & Charlot, S. 2003, 344, 1000
Budavári, T., Szalay, A. S., Connolly, A. J., Csabai, I., & Dickinson, M. 2000, AJ, 120, 1588
Calzetti, D., Armus, L., Bohlin, R. C., Kinney, A. L., Koornneef, J., & Storchi-Bergmann, T. 2000, ApJ, 533, 682
Carollo, C. M. 1999, ApJ, 523, 566
Cole, S., Lacey, C. G., Baugh, C. M., & Frenk, C. S. 2000, MNRAS, 319, 268
Cole, S., et al. 2001, MNRAS, 326, 255
Conselice, C. J. 2003, ApJS, 147, 1
Conselice, C. J., Bershady, M. A., Dickinson, M., & Papovich, C. 2003, AJ, 126, 1183
Conselice, C. J., Blackburne, J., & Papovich, C. 2004a, ApJ, submitted
Conselice, C. J., et al. 2004b, ApJ, 600, L139
Contardo, G., Steinmetz, M., & Fritze-von Alvensleben, U. 1998, ApJ, 507, 497
Corbin, M. R., Urban, A., Stobie, E., Thompson, R. I., & Schneider, a. G. 2001, ApJ, 551, 23
Dalcanton, J. J. & Bernstein, R. A. 2002, AJ, 124, 1328
de Jong, R. S., & Lacey, C. 2000, ApJ, 545, 781
de Vaucouleurs, G., de Vaucouleurs, A., Corwin Jr., H.G., Buta, R.J., Fouque, P., & Paturel, G. 1991 The Third Reference Catalogue of Bright Galaxies, (New York: Springer–Verlag)
Dickinson, M. 2000, Phil. Trans. R. Soc. Lond. A, 358, 2001
Dickinson, M. et al. 2000, ApJ, 531, 624
Dickinson, M., Papovich, C., Ferguson, H. C., & Budavári, T. 2003, ApJ, 587, 25
Driver, S. P., Windhorst, R. A., & Griffiths, R. E. 1995, ApJ, 449, 23
Ellis, R. S. 1997, ARA&A, 35, 389
Fasano, G., & Franceschini, A. 1987, MNRAS, 225, 155
Ferguson, H. C., et al. 2004, ApJ, 600, L107
Förster–Schreiber, N. M. et al., 2004, ApJ, in press (astro–ph/0408077)
Freeman, K. 1970, ApJ, 160, 811
Fruchter, A. S. & Hook, R. N. 2002, PASP, 114, 144
Giavalisco, M., & Dickinson, M., 2001 ApJ, 550, 177
Giavalisco, M., Steidel, C. C., Adelberger, K. L., Dickinson, M., Pettini, M., & Kellogg, M. 1998, ApJ, 503, 543
Giavalisco, M., Steidel, C. C., & Macchetto, F. D. 1996, ApJ, 470, 189
Griffiths, R. E. et al. 1996, in *Examining the Big Bang and Diffuse Background Radiations, proceedings from IAU Symposium 168*, eds. M. C. Kafatos, & Y. Kondo (Dordrecht: Kluwer Academic Publishers), 219
Im, M., Griffiths, R. E., Naim, A., Ratnatunga, K. U., Roche, N., Green, R. F., & Sarajedini, V. L. 1999, ApJ, 510, 82
Im, M. et al. 2002, ApJ, 571, 136
Kuchinski, L. E., Mardore, B. F., Freedman, W. L., & Trewhella, M. 2001, AJ, 122, 729
Kuchinski, L. E., et al. 2000, ApJS, 131, 441
Labbé, I. et al. 2003, ApJ, 591, L95
Lilly, S. J., et al. 1998, ApJ, 500, 75
Lotz, J., Madau, P., Giavalisco, M., Primack, J., & Ferguson, H. C., 2005, in preparation
Lowenthal, J. D., et al. 1997, ApJ, 481, 673.
Marcum, P. M., et al. 2001, ApJS, 132, 129
Marleau, F. R., & Simard, L. 1998, ApJ, 507, 585
Menanteau, F., Abraham, R. G., & Ellis, R. S. 2001, MNRAS, 322, 1
Menanteau, F., et al. 2004, ApJ, in press (astro-ph/0405326)
Mihos, A. C., & Hernquist, L. 1996, ApJ, 464, 641
Mo, H. J., Mao, S., & White, S. D. M. 1998, MNRAS, 295, 319
Mo, H. J., Mao, S., & White, S. D. M. 1999, MNRAS, 304, 175
Moth, P., & Elston, R. 2002, AJ, 124, 1186
Moustakas, L. A., et al. 2004, ApJ, 600, L131
Norberg, P., et al. 2002, MNRAS, 336, 907
Oke, J., Gunn, J., & Hoessel, J. 1996, AJ, 111, 29
Papovich, C., Dickinson, M., & Ferguson, H. C. 2001, ApJ, 559, 620
Papovich, C., Giavalisco, M., Dickinson, M., Conselice, C. J., & Ferguson, H. C. 2003, ApJ, 598, 827 (P03)
Papovich, C., et al. 2004, ApJ, 600, L111
Peacock, J. A. 1983, MNRAS, 202, 615
Porciani, C., & Giavalisco, M. 2002, ApJ, 565, 24
Ravindranath, S., et al. 2004, ApJ, 604, L9
Roberts, M. S., & Haynes, M. P. 1994, ARA&A, 32, 115
Roche, N., Ratnatunga, K., Griffiths, R. E., Im, M., & Neuschaefer, L. 1996, MNRAS, 282, 1247
Roye, E., et al. 2003, "NICMOS Instrument Handbook", Version 6.0, (Baltimore: STScI).
Sawicki, M. & Yee, H. K. C. 1998, AJ, 115, 1329
Shapley, A. E., Steidel, C. C., Adelberger, K. L., Dickinson, M., Giavalisco, M., & Pettini, M. 2001, ApJ, 562, 95
Simard, L., et al. 1999, ApJ, 519, 563
Somerville, R. S., Primack, J. R., & Faber, S. M. 2001, MNRAS, 320, 504
Stanford, S. A., Dickinson, M., Postman, M., Ferguson, H. C., Lucas, R. A., Conselice, C. J., Budavári, T., & Somerville, R. 2004, AJ, 127, 131
Steidel, C. C., Giavalisco, M., Pettini, M., Dickinson, M., & Adelberger, K. L. 1996, ApJ, 462, L17

Steidel, C. C., Adelberger, K. L., Giavalisco, M., Dickinson, M., & Pettini, M. 1999, ApJ, 519, 1
Steinmetz, M. & Navarro, J. F. 2002, New Astronomy, 7, 155
Teplitz, H. I., Gardner, J. P., Malumuth, E. M., & Heap, S. R. 1998, ApJ, 507, L17
Trager, S. C., Faber, S. M., Worthey, G., & González, J. J. 2000, AJ, 120, 165
Trujillo, I., et al. 2004, ApJ, 604, 521
van den Bergh, S., 2002, PASP, 114, 797
van den Bergh, S., Abraham, R. G., Ellis, R., S., Tanvir, N. R., & Glazebrook, K. G. 1996, AJ, 112, 359
van den Bergh, S., Cohen, J. G., & Crabbe, C. 2001, AJ, 122, 611
van Dokkum, P. G., Franx, M., Fabricant, D., Illingworth, G. D., & Kelson, D. D. 2000, ApJ, 541, 95
van Dokkum, P. G., et al. 2004, ApJ, 611, 703
Whitmore, B. C., Zhang, Q., Leitherer, C., Fall, S. M., Schweizer, F., & Miller, B. W. 1999, AJ, 118, 1551
Williams, R. E., et al. 1996, AJ, 112, 1335
Windhorst, R. A. et al. 2002, ApJS, 143, 113
Zepf, S. E., Moustakas, L. A., & Davis, M. 1997, ApJ, 474, L1